Chapter 7

Parametric polarization pulse shaping

So far, this thesis described experiments with femtosecond pulses that were linearly polarized; for the following chapters, light fields with varying polarization states on a fs-timescale will be employed. Coherent control can benefit greatly if the vectorial nature of light is considered, as molecular transition dipole matrix elements contain the scalar product $\boldsymbol{\mu} \cdot \mathbf{E}$. Polarization pulse shaping is still a young, emerging topic in the field of femtochemistry; the contribution of this thesis will be to study the means of two recently developed pulse shaper setups in the time domain and to apply and optimize parametrically shaped polarization pulses on the model system NaK.

7.1 Mathematical tools

7.1.1 Jones Formalism

The Jones formalism, using vectors to represent coherent light fields and matrices for optical elements, is an elegant and practical approach for describing polarized light. As a transverse wave, light can be separated in two perpendicular components

$$\mathbf{E} = \begin{bmatrix} E_x \\ E_y \end{bmatrix} = \mathbf{E_0} \cdot e^{i(kz-\omega t)}. \tag{7.1}$$

The complex vector $\mathbf{E}_0$ is called the Jones vector [135] and can be separated in amplitude and phase[1]

$$\mathbf{E_0} = \begin{bmatrix} a \cdot e^{i\varphi_x} \\ b \cdot e^{i\varphi_y} \end{bmatrix}. \tag{7.2}$$

Jones vectors are often used in a normalized form. For polarized light, the phase difference $\varepsilon = \varphi_y - \varphi_x$ and the field amplitudes determine the polarization state. Linearly polarized light, for example, is written in the normalized form as $P = \begin{bmatrix} 1 \\ 0 \end{bmatrix}$, when horizontally polarized. General, elliptically polarized light is stated as

$$\frac{1}{\sqrt{A^2 + B^2 + C^2}} \begin{bmatrix} A \\ B \pm iC \end{bmatrix}$$

[1] when the slowly varying envelope approximation can be applied

where + stands for right-handed elliptical and − for left-handed elliptical light, with the special case of circularly polarized light $\begin{bmatrix} 1 \\ \pm i \end{bmatrix}$. Linear transformations of polarized light (carried out by optical elements) can be written [136] as a 2×2 matrix $\mathbf{L}$, transforming a light field stated by a Jones vector J by

$$\mathbf{L}J = \begin{bmatrix} l_{11} & l_{12} \\ l_{21} & l_{22} \end{bmatrix} J = J' \tag{7.3}$$

to become the new state J'. For a sequence of linear optical elements in the order $1, 2, \cdots, K$, a compound matrix can be written in the order

$$\mathbf{L} = \mathbf{L}_K \cdots \mathbf{L}_2 \cdot \mathbf{L}_1. \tag{7.4}$$

For example, a linear polarizer at an angle of θ looks like

$$\mathbf{L}_{pol}(\theta) = \begin{bmatrix} \cos^2\theta & \sin\theta\cos\theta \\ \sin\theta\cos\theta & \sin^2\theta \end{bmatrix} \tag{7.5}$$

and a (counter-clockwise) rotation of a Jones vector by the angle of θ can be expressed by the matrix

$$\mathbf{L}_{rot}(\theta) = \begin{bmatrix} \cos\theta & -\sin\theta \\ \sin\theta & \cos\theta \end{bmatrix}. \tag{7.6}$$

A half-wave plate is capable of such a transformation and rotates the polarization by twice the difference between the orientation of the polarization and the angle of the fast axis. The general form of a phase retarder with an optical axis angle of θ that enacts the retardance ϕ an be stated as

$$\mathbf{L}_{PR}(\phi, \theta) = \begin{bmatrix} e^{i\phi/2}\cos^2\theta + e^{-i\phi/2}\sin^2\theta & (e^{i\phi/2} - e^{-i\phi/2})\sin\theta\cos\theta \\ (e^{i\phi/2} - e^{-i\phi/2})\sin\theta\cos\theta & e^{i\phi/2}\cos^2\theta + e^{-i\phi/2}\sin^2\theta \end{bmatrix}. \tag{7.7}$$

A dual-array liquid crystal modulator consists of two (arbitrary) phase retarders which independently exert ϕ_a and ϕ_b. With optical axes aligned at $\pm 45°$ it can be written as $\mathbf{L}_{PR}(\phi_a, 45°) \cdot \mathbf{L}_{PR}(\phi_b, -45°)$. With a horizontally, linearly polarized input pulse P, the dual array modulator gets the form

$$\mathbf{L}_{dual}(\phi_a, \phi_b) = e^{\frac{i}{2}(\phi_a+\phi_b)} \begin{bmatrix} \cos\frac{\phi_a-\phi_b}{2} & i\sin\frac{\phi_a-\phi_b}{2} \\ i\sin\frac{\phi_a-\phi_b}{2} & \cos\frac{\phi_a-\phi_b}{2} \end{bmatrix} \tag{7.8}$$

whereby the common phase term $e^{\frac{i}{2}(\phi_a+\phi_b)}$ must not be neglected (as it is common for Jones formalism) if pulse shaping is to be conducted where different frequencies receive different retardances. A 0° aligned polarizer $\begin{bmatrix} 1 & 0 \\ 0 & 0 \end{bmatrix}$ placed after the two arrays results in

$$\mathbf{L}_{ph+amp} = e^{\frac{i}{2}(\phi_a+\phi_b)} \begin{bmatrix} \cos\left(\frac{\phi_a-\phi_b}{2}\right) \\ 0 \end{bmatrix}, \tag{7.9}$$

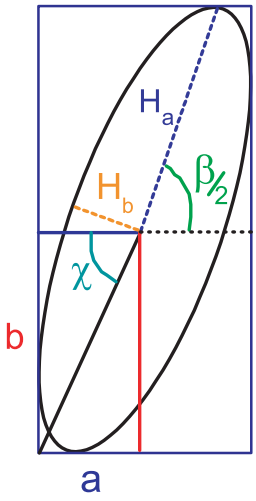

Figure 7.1: Ellipse encoding parameters. The bounding box halves a and b represent the temporal (or spectral) amplitudes in the laboratory system, H_b and H_a are the semi-minor and semi-major axes, respectively, $\beta/2$ is the major axis angle.

which describes the phase- and amplitude shaper (Eq. 3.3) used for the previous chapters. This also means that it can be easily transformed into a phase-and-polarization capable setup, just by removing the polarizer. Before performing pulse shaping using the above described formalism, a few words on how to transform arbitrarily oriented ellipse parameters to amplitudes and phase shifts in the laboratory system.

7.1.2 Ellipse parameters

For a given laboratory system, a bounding box can be drawn around a general ellipse (Fig. 7.1). The relative phase shift ε determines the shape of the ellipse for a given bounding box, similar to how Lissajous figures are constructed. The ellipse parameter set `E` is stated as: $\{I,\ H_{ba},\ \beta/2, hel\}$, whereby I is the intensity, $H_{ba} = H_b/H_a$ the ellipticity[2], or aspect ratio (which is the ratio of minor to major axis), major axis angle (counter-clockwise from the x-axis), and hel as the helicity can also be expressed by the parameters from set `B`: $\{a, b, \varepsilon\}$.

A transformation can be performed by comparing the coefficients of the equations which describe the respective ellipses in both sets, as

$$\left[\frac{x\cos\frac{\beta}{2} + y\sin\frac{\beta}{2}}{H_a}\right]^2 + \left[\frac{y\cos\frac{\beta}{2} - x\sin\frac{\beta}{2}}{H_b}\right]^2 = 1, \tag{7.10}$$

or alternatively,

$$x^2\left(\frac{\cos^2\frac{\beta}{2}}{H_a^2} + \frac{\sin^2\frac{\beta}{2}}{H_b^2}\right) + y^2\left(\frac{\cos^2\frac{\beta}{2}}{H_b^2} + \frac{\sin^2\frac{\beta}{2}}{H_a^2}\right) + 2xy\left(\frac{\cos\frac{\beta}{2}\cdot\sin\frac{\beta}{2}}{H_a^2} - \frac{\cos\frac{\beta}{2}\sin\frac{\beta}{2}}{H_b^2}\right) = 1, \tag{7.11}$$

and

$$\left(\frac{x}{a}\right)^2 + \left(\frac{y}{b}\right)^2 - \frac{2xy\cos\varepsilon}{ab} = \sin^2\varepsilon, \tag{7.12}$$

which also can be written as

$$x^2\cdot\left(\frac{1}{a\sin\varepsilon}\right)^2 + y^2\cdot\left(\frac{1}{b\sin\varepsilon}\right)^2 - 2xy\cdot\frac{1}{a}\cdot\frac{1}{b}\cdot\frac{\cos\varepsilon}{\sin^2\varepsilon} = 1. \tag{7.13}$$

[2] an alternative definition of ellipticity corresponds to the "flattening", defined as $(H_a - H_b)/H_a$

For the transformation, Eq. 7.13 and Eq. 7.10 must be equal, meaning also the three coefficients x^2, y^2 and $2xy$ must be equal:

$$\frac{1}{a^2 \sin^2 \varepsilon} = \frac{\cos^2 \frac{\beta}{2}}{H_a^2} + \frac{\sin^2 \frac{\beta}{2}}{H_b^2} \tag{7.14}$$

$$\frac{1}{b^2 \sin^2 \varepsilon} = \frac{\cos^2 \frac{\beta}{2}}{H_b^2} + \frac{\sin^2 \frac{\beta}{2}}{H_a^2} \tag{7.15}$$

$$\frac{\cos \varepsilon}{\sin^2 \varepsilon} \cdot \frac{1}{a\ b} = \cos \frac{\beta}{2} \sin \frac{\beta}{2} \cdot \Big(\frac{1}{H_b^2} - \frac{1}{H_a^2} \Big). \tag{7.16}$$

Transformation `B` $\rightarrow$ `E` The last equation can also be written as

$$\frac{\cos \varepsilon}{\sin^2 \varepsilon} \cdot \frac{2}{a\ b} = \sin \beta \Big(\frac{1}{H_b^2} - \frac{1}{H_a^2} \Big). \tag{7.17}$$

Eq. 7.14 + Eq. 7.15 equals

$$\frac{1}{\sin^2 \varepsilon} \Big(\frac{1}{a^2} + \frac{1}{b^2} \Big) = \frac{1}{H_a^2} + \frac{1}{H_b^2} \tag{7.18}$$

and Eq. 7.14 - Eq. 7.15 gives

$$\frac{1}{\sin^2 \varepsilon} \Big(\frac{1}{a^2} - \frac{1}{b^2} \Big) = \cos \beta \Big(\frac{1}{H_a^2} - \frac{1}{H_b^2} \Big) \tag{7.19}$$

Eq. 7.17 / (Eq. 7.14 - Eq. 7.15) eliminates H_a and H_b:

$$2ab \cos \varepsilon = (a^2 - b^2) \tan \beta. \tag{7.20}$$

Solving (Eq. 7.18 + Eq. 7.19) - which eliminates H_b results in

$$H_a^2 = \frac{2a^2 b^2 \sin \varepsilon}{a^2 + b^2 + (b^2 - a^2)/\cos \beta}, \tag{7.21}$$

similarly, H_b^2 yields

$$H_b^2 = \frac{2a^2 b^2 \sin \varepsilon}{a^2 + b^2 + (a^2 - b^2)/\cos \beta}. \tag{7.22}$$

Eq. 7.20 can be used to eliminate β using the relation $\cos(\arctan \zeta) = 1/(\sqrt{1 + \zeta^2})$, so for the individual ellipse major axes

$$H_{a,b} = \sqrt{\frac{2a^2 b^2 \sin^2 \varepsilon}{a^2 + b^2 \mp (a^2 - b^2)\sqrt{1 + \frac{4a^2 b^2 \cos^2 \varepsilon}{(a^2 - b^2)^2}}}}, \tag{7.23}$$

using $-$ for H_a and $+$ for H_b. The major axis angle $\beta/2$ becomes

$$\frac{\beta}{2} = \frac{1}{2} \arctan \frac{2ab \cos \varepsilon}{a^2 - b^2} \tag{7.24}$$

whereby for cases when $a^2 - b^2 < 0$, $\pi/2$ has to be added to $\beta/2$, and the intensity is simply $I = a^2 + b^2$.

Transformation `E` $\rightarrow$ `B` The inverse transformation eliminates a and b from the equation set 7.14 - 7.17 and is of practical importance when an electrical field has to be constructed from temporally varying angles, ellipticities, and intensities. The bounding box diagonal (see Fig. 7.1)

$$\chi = \frac{1}{2} \arccos \left[\cos \beta \cos \left(2 \arctan H_{ba} \right) \right] \tag{7.25}$$

can be used to derive the field amplitudes a and b, employing the intensity I as

$$\begin{aligned} a^2 &= I \cos^2 \chi \\ b^2 &= I \sin^2 \chi \end{aligned} .$$

The phase shift between the x- and y-component can be derived by eliminating a and b from the component comparison 7.14 - 7.17, leading to

$$\varepsilon = \pm \arctan \frac{\tan \left(2 \arctan H_{ba} \right)}{\sin \beta}, \tag{7.26}$$

where the sign has to be selected for left (-) or right handed (+) polarized light. To yield a continuous ε, π has to be added if the major axis angle $\beta/2$ is situated in the second or fourth quadrant. To recreate the electrical field, the phase sum $\varphi_{sum} = \varphi_x + \varphi_y$ is an easy-to-handle parameter as $\varphi_x = \frac{1}{2}(\varphi_{sum} - \varepsilon)$ and $\varphi_y = \frac{1}{2}(\varphi_{sum} + \varepsilon)$, and is also sufficient to fully determine an electrical field when the fast oscillating part is incorporated.

7.1.3 Parametric polarization transients

A polarization state is denoted by the phase shift between the x and y component of the electrical field (Eq. 7.2).

For a demonstration, a double pulse[3] is constructed by superposing temporal fields like

$$\mathbf{E}_{out}(t) = \mathbf{E_1}(t) + \cdots + \mathbf{E}_N(t) \tag{7.27}$$

whereby one sub pulse has the same zero order phase for both field components, and for the other[4] the field components differ by $\pi/2$, which is shown in Fig. 7.2 (a). Fig. 7.2 (b) shows the electrical field vector, visualized in a three-dimensional way, whereby the projections to the walls are identical to the constituting fields (a). The sub pulse having equal x- and y-intensities and no relative phase shift results in a linearly polarized pulse, tilted by 45°. The sub pulse with a $\pi/2$ relative phase shift yields a circular pulse, where the rotational direction (helicity) of the field vector can be tracked by following the field lines in time (see arrows). Fig. 7.2 (c) shows the spectral amplitudes of the x- and y-component[5] and shows that the spectra are shifted with respect to each other. It is obvious that in order to create complex temporal fields by superposition, the common phase offsets of x- and y-fields must not be omitted like for the normalized and phase-stripped Jones formalism. The

[3] λ_0=800 nm, $\Delta\lambda$=100 nm, Δt_{FWHM}=9.47 fs

[4] similarly seen in the third row of Fig. 6.5

[5] which are similar to Fig. 6.5 where different b_0's were applied

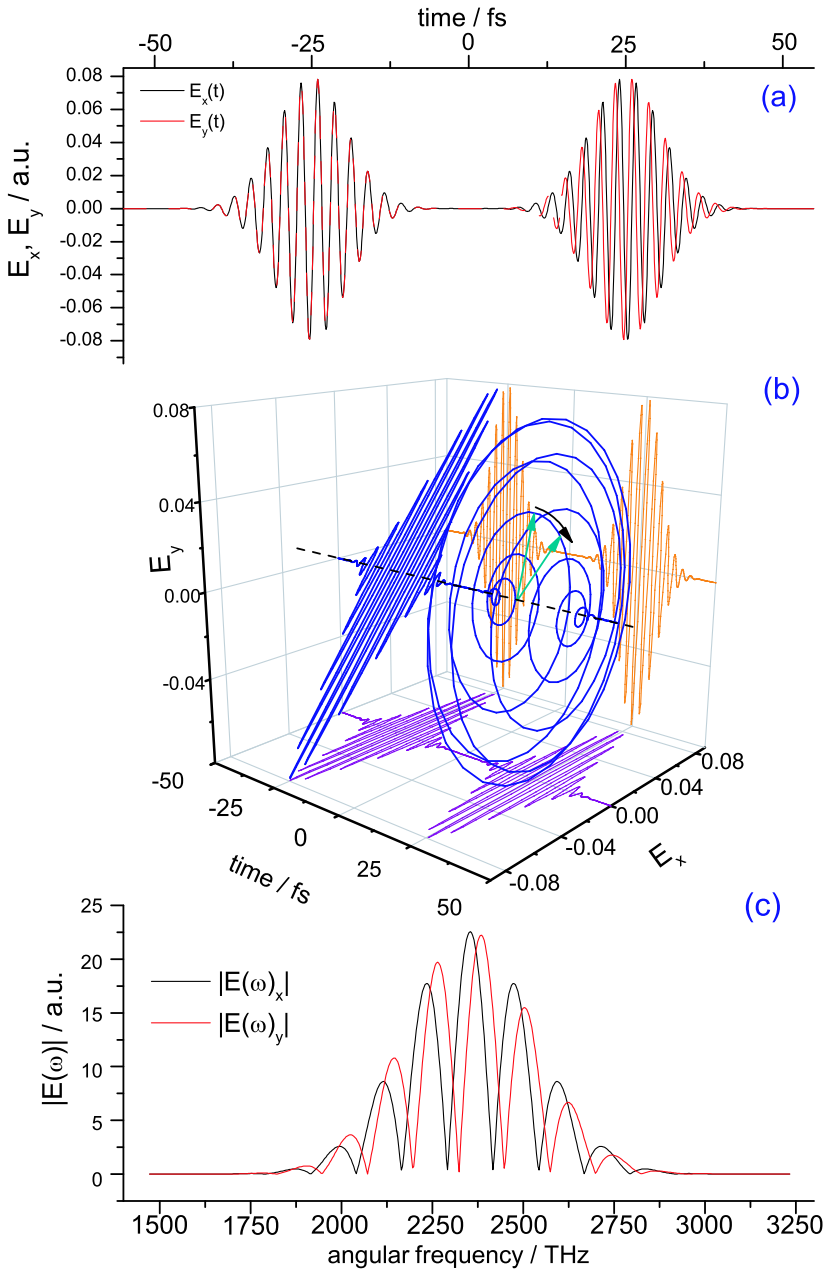

Figure 7.2: Simulation of a linear (45°) / circular double pulse sequence, (a) with a simulated electrical field, (b) as 3D representation including the field projections, and (c) as the spectral amplitudes.

phase of a non-vanishing component can be chosen to act as an absolute reference allowing to define a difference phase $\varepsilon = \varphi_y - \varphi_x$ for every point in time. For this work, the x-axis chosen, which means that the zero order phase for the x-component stays unchanged ($b_{0x} = b_0$) and only the y-component is shifted to obtain a polarized field ($b_{0y} = b_0 + \varepsilon$). The calculation of a filter function to obtain a field with a varying polarization from a linearly polarized input field $E_{in}(\omega)$ does not differ in essence from the respective calculations for linearly polarized pulses. Following the steps from Section 6.3.1, a general superposition of, this time, N vectorial fields in the frequency domain can be expressed as

$$\mathbf{E}_{out}(\omega) = \mathbf{E_1}(\omega) + \cdots + \mathbf{E}_N(\omega) = \sum_N \mathbf{E}_N(\omega) = E_{in}(\omega) \cdot \sum \tilde{\mathbf{H}}_N(\omega), \tag{7.28}$$

similar to Eq. 7.27. The vectorial filter function $\tilde{\mathbf{H}}_N(\omega)$ (the filter for one sub pulse) is factorized in

$$\tilde{\mathbf{H}}_N(\omega) = \begin{bmatrix} R_{N,x}(\omega) \cdot e^{i\phi_{N,x}(\omega)} \\ R_{N,y}(\omega) \cdot e^{i\phi_{N,y}(\omega)} \end{bmatrix} \tag{7.29}$$

and, similarly, the sum of all N sub pulse's filter functions yield a total filter

$$\tilde{\mathbf{H}}(\omega) = \sum_N \tilde{\mathbf{H}}_N(\omega) = \begin{bmatrix} R_x(\omega) \cdot e^{i\phi_x(\omega)} \\ R_y(\omega) \cdot e^{i\phi_y(\omega)} \end{bmatrix} \tag{7.30}$$

which can optionally be transformed to the time domain

$$\tilde{\mathbf{h}}(t) = \frac{1}{2\pi} \int d\omega \tilde{\mathbf{H}}(\omega) e^{i\omega t} \tag{7.31}$$

in order to create temporal fields as

$$\mathbf{E}_{out}(t) = E_{in}(t) \cdot \sum \tilde{\mathbf{h}}_N(t). \tag{7.32}$$

From Eq. 7.30 it becomes clear that a pulse shaper setup which fully controls the phase, amplitude, and polarization must be capable of independently modulating the x- and y-field component's phase and amplitude.

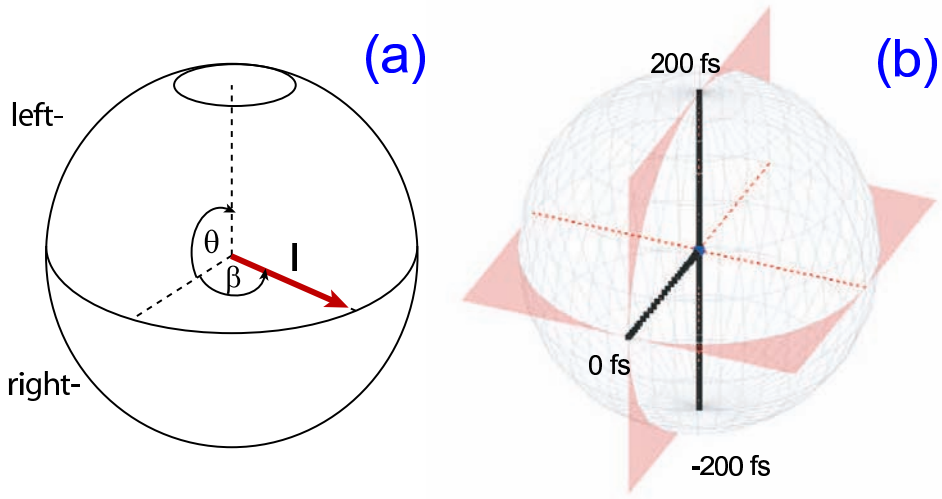

Figure 7.3: (a) Poincaré sphere, extended by employing the intensity as radial component $r = I$ in order to visualize temporally changing polarization states. (b) The T-shaped path below the surface represents a temporally separated triple pulse, evolving from right-circular →linear/0° →left-circular. The sectional planes and the dashed cross are used to point out a particular detail on the path.

7.1.4 Extended Poincaré representation

The Poincaré sphere representation (see Fig. 7.3 (a)) is a useful way of visualizing polarization states [137]. A state is mapped on the surface of a sphere, whose coordinates are closely related to the ellipse parameters. To cover all of the sphere, the major axis angle times two, β, corresponds to the longitude and the ellipticity determines the latitude[6] as $\theta = \pm 2 \arctan H_{ba}$, where $-$ stands for right-handed light (southern hemisphere) and $+$ for left-handed light (northern hemisphere). Polarization states which change in time (or in the frequency domain) can be represented as paths on the sphere, with additional temporal/spectral markers. The development of femtosecond pulses on the Poincaré sphere was treated in detail in Ref. [138], where also the temporal derivatives, which represent the maximal "speed" on the sphere, were derived.

However, the parameters discarded for the usual representation are intensity and phase. For this work, the intensity I will be incorporated to the description by representing the radial component. The transformed paths now, mostly, lie inside the sphere when the maximal temporal intensity is normalized to lie on the surface. For a better visualization, a transparent sphere (see Fig. 7.3 (b)) is drawn for this thesis, with additional sectional planes and a cross-like cursor (dashed) to indicate the point of interest. The depicted sphere has an embedded T-shaped path, which corresponds to a triple pulse which starts at zero intensity, becomes right-circular at t=-200 fs, decreases to zero intensity again, changes into to a linear pulse at t=0 fs at 0°, then again passes zero intensity, and finally becomes left circular (t=200 fs) before vanishing at the center of the sphere, where $I = 0$. The chosen representation is also useful for experimental reasons when noisy signals have to be visualized, as in

[6] for $0 < H_{ba} < 1$

a pure surface depiction every point in time corresponds to one point on the sphere, no matter how low the intensity is and how noisy the corresponding polarization states are.

7.2 Historical perspective

Experimental polarization pulse shaping can be seen as the effort to construct setups that enact setup-dependent filters $\tilde{\mathbf{H}}(\omega)$ upon light fields in order to obtain control over polarization transients. Until today, there has been a steady improvement of the first pulse shaper setups capable of addressing the polarization. Historically, the first publication carrying out polarization shaping with liquid crystal modulators was published by Wefers and Nelson in 1995 [16]. They used a newly developed dual array modulator with two independently controllable arrays, arranged in a $\pm 45°$ fashion (which corresponds to $\mathbf{L}_{dual}$ - Eq. 7.8), and was capable of producing polarization ellipses with restricted major axis angles. Their setup, a 4-f configuration with 1800 lines/mm gratings caused a very strong polarization dependent diffraction efficiency, with an y-reflectivity of $<1\%$.

A solution to the grating problem was presented by Gerber/Brixner six years later [17] by placing glass plates at the Brewster angle in the beam in order to diminish the more intense component to match the weaker one, with an additional total loss due to the added material. Their "equalized" polarization setup was the first to be employed in a coherent control experiment of this type, optimizing the ionization efficiency of potassium molecules [139], resulting in an improved optimization factor compared to phase-only modulation. This setup was also utilized by other groups to experiment on aligned iodine molecules [140] or to control the angular momentum distribution in atoms [141]. A more recent study on controlling nano-structures with polarization shaped pulses [142] uses so-called volume phase holographic (VPH) gratings [143, 144] which have a greatly reduced polarization dependent reflectivity for a given central wavelength.

In the field of fiber optics, transformation of polarization states using three subsequent nematic crystal cells aligned at $0°/45°/0°$ [145] could be successfully employed to compensate for polarization-mode dispersion (PMD) and polarization dependent loss (PDL), which are bottlenecks in high-speed optical telecommunication systems. Such setups consist of three sequential cells, which are able to transform arbitrary input polarization states into any output state. A double-layer LCM was used in a $90°/\text{-}45°$ arrangement in Ref. [146] which allowed to compensate for PMD and PDL within a certain wavelength range.

For pulse shaping, a major improvement was made recently by Polachek et al. [19], who sequentially combined a standard double array modulator, with a single array modulator which enabled the polarization ellipse's major axis to be rotated freely in the spectral domain.

7.3 Serial setup

The polarization setups known from literature still leave room for improvement, due to their inability to manipulate the spectral *amplitude*, ruling out full control of

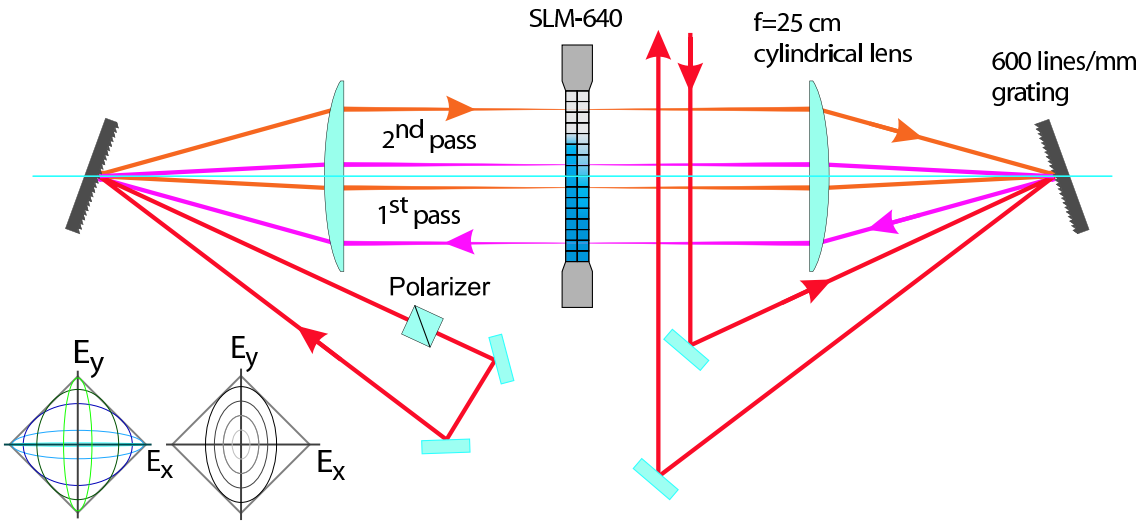

Figure 7.4: Serial setup which modulates phase, amplitude, and polarization in a double-pass configuration. Left bottom insets: sketches of achievable polarization ellipses, which are also scalable by amplitude modulation.

the electrical field. This shortcoming is addressed by two new polarization shaping setups (nicknamed "serial" and "parallel" setup) which were co-developed with M. Plewicki [28] and F. Weise [147] in the frame of this work. M. P.'s work focuses on the shaper's properties and capabilities in the frequency domain; in this thesis, the time domain is emphasized.

The serial setup is a double-pass configuration, effectively employing four liquid crystal arrays, and the input pulse travels twice through the SLM-640 (which is spacious enough to allow aligning such a beam path), as outlined in Fig. 7.4. The beam path is indicated by the arrows, whereby first, the "lower" part is traversed. When the pulse leaves the pulse shaper for the first time, it passes through a horizontally aligned polarizer which enacts the amplitude modulation, the possibility to additionally modulate the phase in the first pass was not incorporated. Then, the pulse is sent back through the shaper for a second time when the phase and polarization are modulated. The insets in Fig. 7.4 shows the possible spectral polarization states, with the major axis of the resulting spectral ellipses pointing either in x- or y-direction. The first-pass amplitude modulation can be employed to scale the ellipse's area while upholding its aspect ratio.

The serial setup, as an optical element, can be described by a sequence of Jones matrices using Eqs. 7.8 and 7.5 as

$$\mathbf{L}_{ser} = \underbrace{\mathbf{L}_{dual}}_{second\ pass} \cdot \mathbf{L}_{pol}(0°) \cdot \underbrace{\mathbf{L'}_{dual}}_{first\ pass} . \tag{7.33}$$

The complex, vectorial output field of the serial setup is therefore

$$\begin{bmatrix} E_{out,x} \\ E_{out,y} \end{bmatrix} = E_{in}(\omega) \underbrace{R(\omega)}_{amplitude} \underbrace{e^{\frac{i}{2}(\phi_a(\omega)+\phi_b(\omega))}}_{phase} \underbrace{\begin{bmatrix} \cos\frac{\phi_a(\omega)-\phi_b(\omega)}{2} \\ i\sin\frac{\phi_a(\omega)-\phi_b(\omega)}{2} \end{bmatrix}}_{polarization} = E_{in}(\omega)\cdot\tilde{\mathbf{H}}^{ser}(\omega). \tag{7.34}$$

which can also be written as the effect of a complex, vectorial filter function $\mathbf{H}_{ser}(\omega)$ on a given linear input field. In the equation, $E_{in}(\omega)$ is the linearly polarized input pulse and $\phi_a(\omega)$ and $\phi_b(\omega)$ are the frequency dependent phase retardances induced by the second pass. The first-pass amplitude modulation is collected in the term $R(\omega) = \cos\frac{\phi_{a'}(\omega)-\phi_{b'}(\omega)}{2}$ with $\phi_{a'}(\omega)$ and $\phi_{b'}(\omega)$ being the respective first-pass retardances. Depending on the difference retardance, defined as $\Delta\phi = \phi_a - \phi_b$, for this work, the respective frequency component consists of either left ($\sin\frac{\Delta\phi}{2} < 0$) or right ($\sin\frac{\Delta\phi}{2} > 0$) handed, polarized light.

7.3.1 Grating effects

To overcome the orientation dependent reflection effectivity of the employed gratings using the first-pass amplitude is a practical advantage; overcoming the need for additional elements like glass plates at the Brewster angle [148] which reduces the output power significantly and introduces a wavelength dependence[7], or transparent holographic gratings [143, 144, 142] which are expensive and also have an efficiency drop off the custom-tailored wavelength.

Ellipticity selector. An ellipticity (minor to major axis ratio) "selector", as shown in Fig. 7.5 (b) can be useful for cases where symmetrical pulses forms are not required. Finding the right ellipticity can be achieved by using the look-up table $\Delta\phi_{adapt} = \sqrt{P_x/P_y}$, drawn in Fig. 7.5 (b). For example, if a circular polarization is required (dashed lines), the experimentally obtained value would be $\Delta\phi_{adapt}$= 0.518 π instead of 0.5 π.

Amplitude as grating correction. As the ellipticity depends on the difference retardance, the precompensation in the first pass must be performed according to $\Delta\phi$ of the second pass. This can be done either for all pixels simultaneously for unshaped pulses, or on a pixel-per-pixel basis, if more complex waveforms are to be produced[8]. The grating efficiency can be determined by recording the output power while scanning the difference retardance $\Delta\phi$ of the two arrays (denoted as P_{WO}). To obtain the correction function it is enough to invert and then normalize $P_{WO}(\Delta\phi)$ in Fig. 7.5 and use it as a look-up-table[9] for every pixel. The obtained table $F(\Delta\phi)$ then provides corrective factors to be multiplied with the respective transmission values which are to be applied.

[7] due to the wavelength dependent Brewster angle, causing a changing attenuation over larger bandwidths

[8] such as Fig. 7.11

[9] an analytical function is derived in Ref. [28]

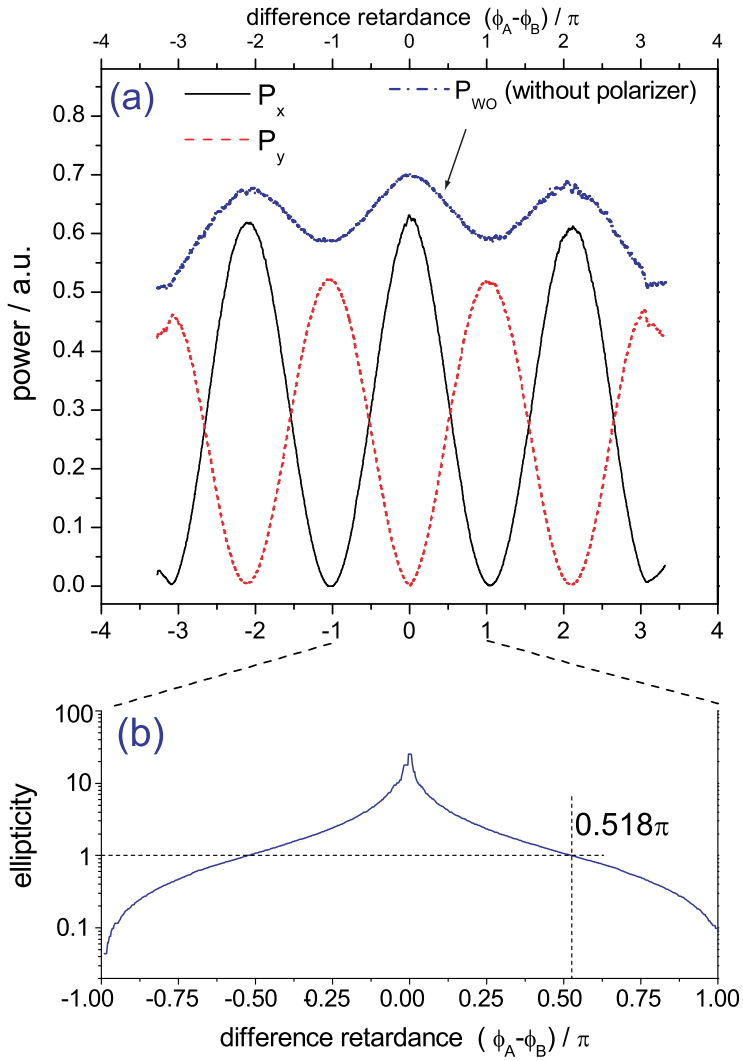

Figure 7.5: (a) Grating efficiency scans (taken from [28]), and ellipticity selector (b) for equalizing the grating effect. With 600 lines/mm gratings, the differences are only about 15 % when placing an x- or y-oriented polarizer after the shaper setup (lines labelled P_x and P_y). P_{WO} is a scan performed without polarizer.

7.3.2 Temporal pulse forms with the serial setup

The two questions: "what can I do with the serial setup" and "how can I construct a desired waveform with the serial setup" have to be treated separately and with some creativity, because an analytical inversion of Eq. 7.34 (which would answer the second question) is not physically feasible, as will be shown next.

When comparing $\tilde{\mathbf{H}}^{ser}(\omega)$ from Eq. 7.34 to the general solution Eq. 7.30 it becomes obvious that the serial setup does not provide absolute control over phase, amplitude, and polarization. First of all, the amplitude filter $R(\omega)$ from Eq. 7.34 does not fulfill the "vectorial" nature from Eq. 7.30, it can be looked upon as scalar multiplier to the input pulse's envelope. The terms which determine the polarization

$$\begin{bmatrix} \cos\frac{\phi_a-\phi_b}{2} \\ i\sin\frac{\phi_a-\phi_b}{2} \end{bmatrix} \tag{7.35}$$

are coupled in x and y-direction which means there can be no independent, orthogonal polarization manipulation. The imaginary unit in the y-component furthermore locks the phase difference between the components to $\pm 90°$, leading to fixed major axis angles with $0°$ and $90°$, which becomes apparent when comparing with the general form of the Jones vector $\begin{bmatrix} A \\ \pm iB \end{bmatrix}$ of such polarization ellipses.

Inverting the Serial Setup Equation. With the described limitations of the serial setup the question arises which kind of temporal pulse forms are feasible. A calculation should start with the desired field $\mathbf{E}_{out}$ and must result the retardances ϕ_a and ϕ_b, and the first-pass amplitude $R(\omega)$. Without further considerations, one can start by solving the equation set Eq. 7.34 for the retardances ϕ_a and ϕ_b. Assuming the retardances ϕ are complex, the general solution is

$$\begin{aligned} \tilde{\phi}_a(\omega) &= -i\ln\tfrac{E_{out,x}(\omega)+E_{out,y}(\omega)}{R(\omega)E_{in}(\omega)} = -i\ln\tfrac{\tilde{H}_x(\omega)+\tilde{H}_y(\omega)}{R(\omega)} \\ \tilde{\phi}_b(\omega) &= -i\ln\tfrac{E_{out,x}(\omega)-E_{out,y}(\omega)}{R(\omega)E_{in}(\omega)} = -i\ln\tfrac{\tilde{H}_x(\omega)-\tilde{H}_y(\omega)}{R(\omega)} \end{aligned} . \tag{7.36}$$

Practically, a single liquid crystal element can not produce an imaginary retardance, therefore, the general solution is experimentally not feasible. There is a procedure in the literature [149, 150] describing an experimental feedback routine to obtain customized polarization profiles which, however, is time-consuming and seems unfeasible for this work, as the intended integration of tailored pulse shaping into an evolutionary algorithm demands that a few thousand pulse forms have to be tested within a limited time frame. Using only the real parts of the retardances

$$\phi(\omega)_{a,b} = \Re\left[-i\ln\frac{E_{out,x}(\omega)\pm E_{out,y}(\omega)}{R(\omega)E_{in}(\omega)}\right] = \Re\left[-i\ln\left(\tilde{H}_x(\omega)\pm\tilde{H}_y(\omega)\right)\right] \tag{7.37}$$

is experimentally feasible, but has of course consequences to the obtained field. The advantage is that this step allows to eliminate $R(\omega)$ from the equation as it comprises a purely imaginary contribution, which, for practical purposes, provides some freedom in choosing an amplitude.

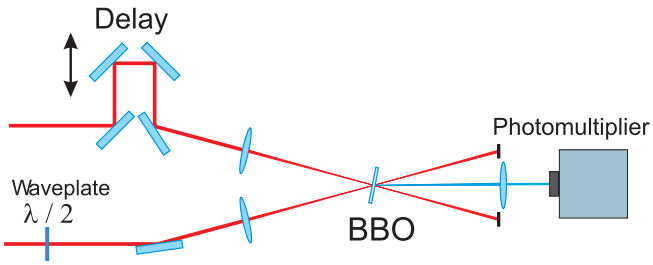

Figure 7.6: TRE-like detection scheme for polarized pulse forms, which are rotated by a $\lambda/2$-wave plate and then overlaid with a reference pulse in a BBO crystal in order to obtain a set of SFG-CC traces for different angles.

With Eq. 7.37 it is possible to calculate the frequency dependent retardances $\phi_a(\omega)$ and $\phi_b(\omega)$ obtained for a desired field $\mathbf{E}_{out}$. The result is, however, a different field $\mathbf{E}'_{out}$

$$\begin{bmatrix} E'_{out,x} \\ E'_{out,y} \end{bmatrix} = \frac{1}{2} E_{in}(\omega) R(\omega) \begin{bmatrix} e^{i\Im[\ln(\tilde{H}_x - \tilde{H}_y)]} + e^{i\Im[\ln(\tilde{H}_x + \tilde{H}_y)]} \\ e^{i\Im[\ln(\tilde{H}_x + \tilde{H}_y)]} - e^{i\Im[\ln(\tilde{H}_x - \tilde{H}_y)]} \end{bmatrix} \tag{7.38}$$

where $\Im$ stands for imaginary part. It is still possible to preselect an adequate $\mathbf{E}(\omega)$, which needs only real valued retardances; such fields are, however, strongly restricted[10]. In the following, fields which were experimentally generated using the feasible solution of Eq. 7.37 will be discussed.

7.4 Experimental realization

With all mathematical tools in place, in the following, a range of experimentally obtained polarization pulses will be presented and the procedure to measure, retrieve, and visualize customized polarization pulse shapes will be explained in a step-by-step manner. For the analysis, double pulses[11] with intended $\Delta t = 500$ fs, consisting of a 90°-linear pulse at t_0, followed by a circular pulse at t_1 will be generated by the serial setup, for now, without employing the first-pass amplitude.

7.4.1 Pulse detection

For acquiring the polarization transients, the same detection setup as described in Sec. 3.4 with sum-frequency generated light from a polarization selective (due to phase matching conditions) BBO crystal is employed. The new element used to characterize the polarization is a half-wave plate to rotate the polarized pulse. The technique to measure an array of SFG-CCs is similar[12] to TRE (time resolved ellipsometry) [151]. The more SFG-CCs are recorded within a reasonable angular range [-90°,90°] the more exact the retrieval will be, although three projections (points) are sufficient to determine the shape (but not the helicity) of an ellipse. The most sensitive parameter to measurement noise is the ellipticity, if the polarization state is near-linear and the intensity is low. An array of SFG-CC traces will be used

[10] one example will be discussed later in Fig. 7.17

[11] $R_1^2 = R_2^2$, at λ_0=790 nm and a FWHM of 25 nm, no amplitude modulation was yet applied, using the grating equalizing described in Sec. 7.3.1

[12] without the additional recording of all the traces through a quarter wave plate to determine the helicity

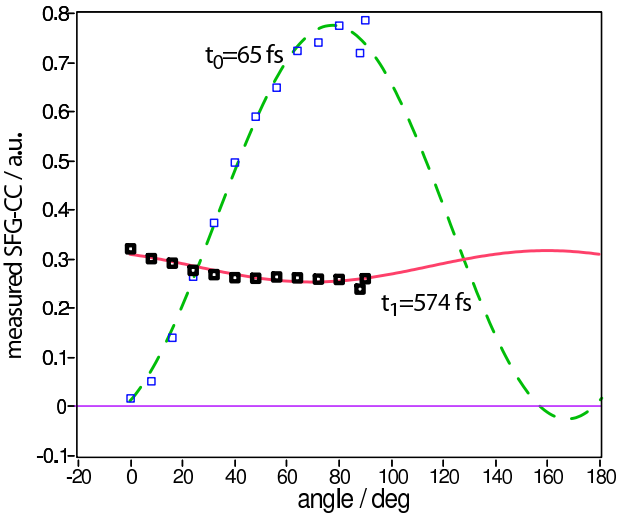

Figure 7.7: Fitting angle dependent projection intensities (see Eq. 7.39); demonstrated for two points in time of the pulse shown in Fig. 7.8. To avoid negative intensity values, as occurred at t_0=65 fs (quasi-linear, dashed line), a higher weight can be given to the lowest points for the fit. Curve (b) at t_1=574 fs (straight line) shows a near-circular state (H_{ba}=0.893).

to plot the temporal course of the ellipticity $H_{ba}(t)$, major axis angle $\beta(t)/2$, and total intensity $I(t)$.

7.4.2 Ellipse parameter fits

The squared projection of a polarization ellipse to a particular angle can be determined[13]. The calculation for set `B`: $\{a, b, \varepsilon\}$ will be given in Sec. 9.3.1 having a sinusoidal angular dependence

$$I_{SFG}(\alpha, t) = a_0(t) + a_1(t) \cdot \sin\left(2\alpha + a_2(t)\right), \tag{7.39}$$

with α as the angle of the projection, a_0 as the sine offset, a_1 as the multiplier, and a_2 as the phase shift.

Fig. 7.7 shows the angular dependence of the intensity for two points in time, where at t_1=574 fs the amplitude of the sine is quite small, resulting in a near-circular pulse. At t_0=65 fs, a quasi-linear polarization state is measured, with the additional problem that the fit curve reaches negative intensities. As the ellipticity is defined as the square root of the ratio of the minimal to maximal value, the problem arises how to reliably determine near-linear states. A way of dealing with this issue is using different fit weightings, favoring the data points with lower values. If the weighting fails, data processing of particularly difficult regions might be necessary, including (in order of preference): low pass filtering (FFT smoothing), a lower cutoff (eliminating negative signals), a baseline offset, slight pulse-peak centering (of the order of a few femtoseconds), artificial noise, and a weighting of the highest values.

7.4.3 Fit coefficient transcriptions

The linear and circular nature of the main pulses (at t_0=65 fs and t_1=574 fs) can also be made out from the SFG-CC projections in Fig. 7.8 (a), whereby the linear pulse's SFG-CC shows one trace that reaches near-zero intensity, and for the supposed circular pulses, all traces overlap to a good degree which, except for the side pulse

[13] a detailed derivation for set `E` is provided by Ref. [28]

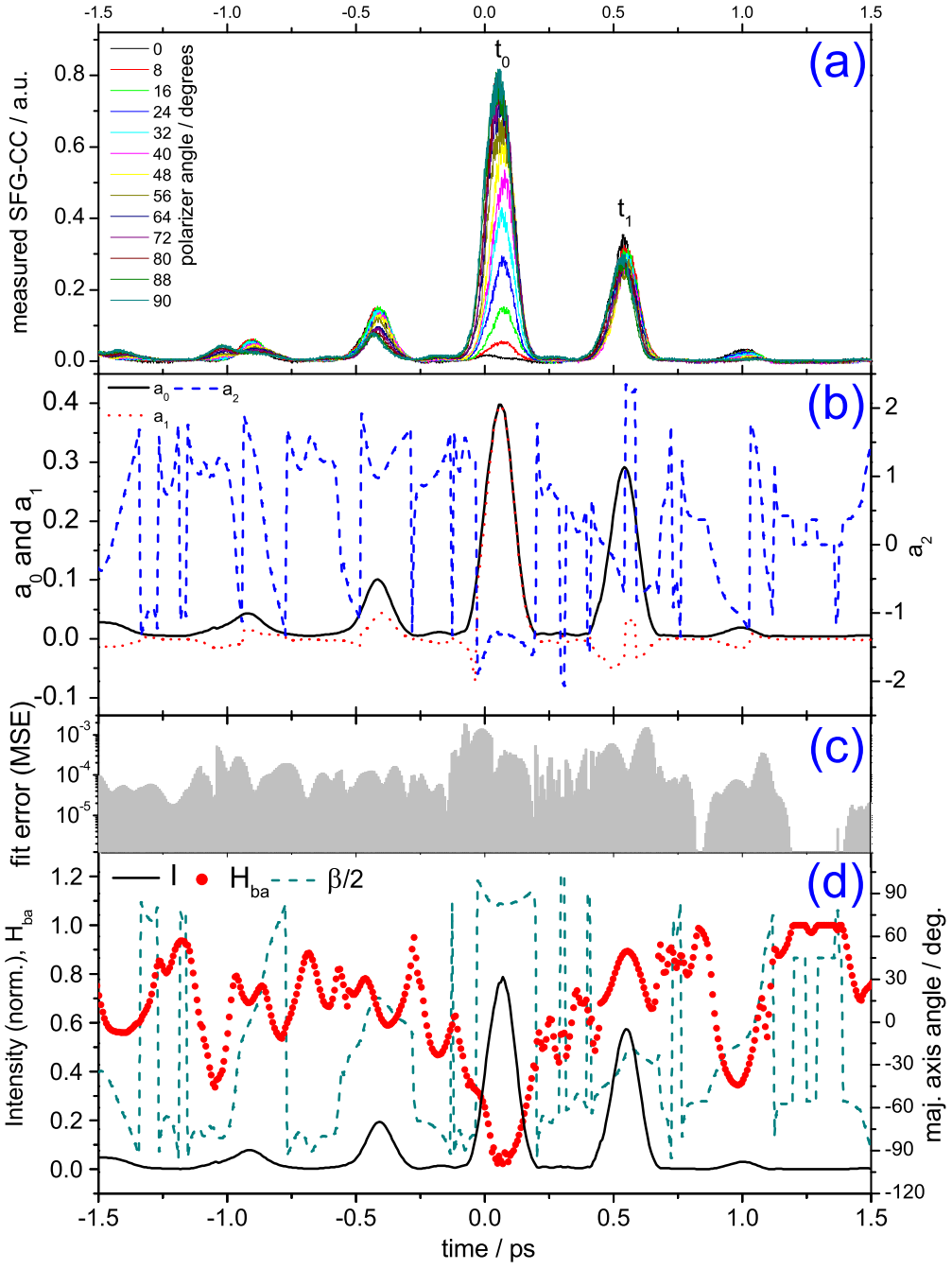

Figure 7.8: Double pulse with an intended Δt=500 fs. (a) SFG-CC measurements from 0 to 90° in steps of 8°, (b) results for the parameters a_0, a_1, and a_2 for the sine-fit (using Eq. 7.39), (c) fit mean squared error, (d) resulting polarization ellipse parameters, using the transcriptions of Eq. 7.40.

at t=-408 fs, is a good agreement with the desired pulse form. The result of fitting the traces using Eq. 7.39 is displayed in Graph (b), displaying $a_0(t)$, $a_1(t)$, and $a_2(t)$. Graph (c) provides the fit mean squared error, which can be used to assess the reliability of particular points in time.

To uniquely transform the fit parameters to ellipse parameters, and restrain them to the ranges $H_{ba}: [0,1]$ and $\beta/2: [-90°, 90°]$, the following transcriptions (using the auxiliary variables η_1 and η_2) are to be carried out.

$$\eta_1 = \sqrt{\frac{a_0 - |a_1|}{a_0 + |a_1|}} \tag{7.40}$$

$$\eta_2 = \begin{cases} a_2 & a_1 < 0 \\ a_2 + \pi & a_1 \geq 0 \end{cases}$$

$$\beta/2 = \begin{cases} \frac{1}{2}(\frac{\pi}{2} - \eta_2) & \eta_1 \leq 1 \\ -\frac{1}{2}\eta_2 & \eta_1 > 1 \end{cases}$$

$$H_{ba} = \begin{cases} \eta_1 & \eta_1 \leq 1 \\ 1/\eta_1 & \eta_1 > 1 \end{cases}$$

$$I = 2a_0$$

The above stated conversions lead to the final, temporal parameter courses, plotted in Fig. 7.8 (d). The intensity is still convoluted with the reference pulse which broadens it in time; this could for example be addressed by deconvolution[14]. The angles for the linear pulse at t_0 (desired 90°, measured 82.7 °) and ellipticities (minimal $H_{ba} <$ 0.021) were at a quite good agreement, the same can be said for the circular pulse at t_1= 574 fs (maximal H_{ba}=0.893 at -20°). The side pulse at t=-408 fs has 1/4 of the main, linear pulse's intensity and lies at 16.9° with an H_{ba} of 0.65.

7.4.4 3D amplitude/Poincaré representation

A pulse form can be represented as a path in the extended Poincaré description (see Sec. 7.1.4). To point out the two main pulses and one side pulse, three spheres are plotted with identical paths, but with different sectional planes that mark the corresponding sub pulses (Fig. 7.9 (a)-(c)). The ideal case for the linear/circular double pulse would be a watch-hand like path[15] starting at the sphere's center; where one finger (representing the linear pulse) points at the equator (at 0° latitude), and the other straight to the north pole. As the helicity was not explicitly determined (only implicitly, by incorporating it to the desired pulse form), the respective trails could also be situated in the other hemisphere. The measured path deviates from the ideal path to some degree and exhibits a shoelace-like form, meaning that the maximal temporal intensities are reached differently at the rising and falling edges. The maximal intensity at the peak of the linear sub pulse is marked by an arrow in Sphere (b). The main circular pulse does not fully reach the surface as it has a

[14] A method of retrieving deconvoluted intensity profiles using an evolutionary algorithm will be introduced in Chapter 9.

[15] similar to the T-shape in Fig. 7.3 (b) without the lower T-bar

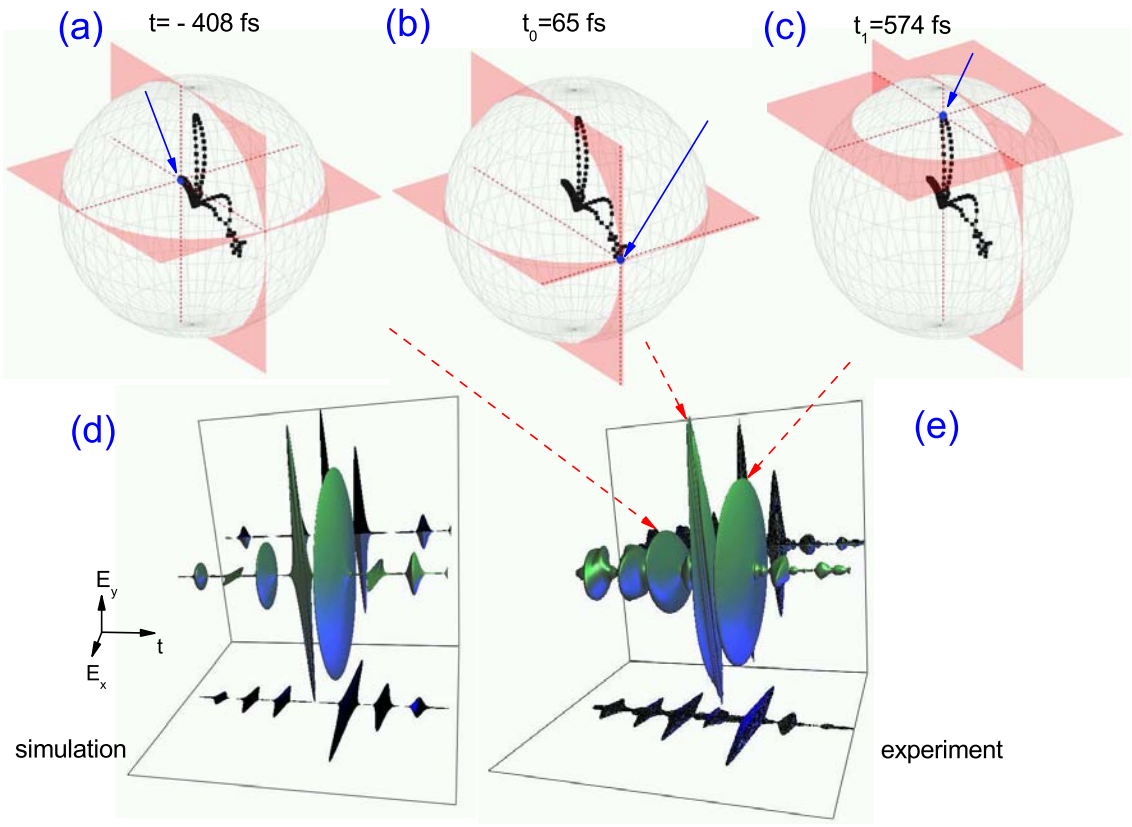

Figure 7.9: (a)-(c) Extended Poincaré representation of an experimental $\Delta t = 500$ fs linear/circular double pulse generated by the serial setup. Sphere (a) indicates the small sub pulse, (b) highlights the main linear pulse, and (c) the near-circular pulse. Bottom row: 3D plot of the temporal amplitude (arbitrary colors) where (d) is a simulation and (e) originates from experimental data. The dashed arrows connect the Poincaré spheres with the respective sub pulses. The sphere is rotated azimuthally by 180° in order to show the main pulses at the front.

reduced intensity compared to the linear pulse - see Sphere (c). The side pulse at t=-408 fs - Sphere (a) - is depicted as a small, upward tail[16].

Three dimensional representations of the temporal amplitude (or even the electrical field) are a visually pleasing way of delivering the encoded information. Fig. 7.9 shows a comparison of simulation (d) and measured pulse form (e). To get more insight, the projections to the respective planes are drawn as black shadows. The Poincaré representations, marking the sub pulses, are linked to the 3D plots by the dashed (red) arrows. The simulation (d) (using Eq. 7.38) is very similar to the measured pulse form in shape. The most significant (visual) difference is the increased temporal width of the experimental pulses, which is due to the convolution with the reference pulse, and a higher energy content of the side pulses than the simulation states. The (larger) side pulses are not an experimental artifact, but have their origin within the restrictions of the serial setup[17]. The simulation also shows that the side pulses alternate in a periodic linear/circular fashion, mimicking the behavior of the intended main pulses.

7.4.5 Spectral properties

The pulse spectra of a similar, linear/circular double pulse[18] with Δt=400 fs will be discussed next. The serial setup requires (Eq. 7.34) for every frequency ω

$$E_{x,out}(\omega)E^*_{x,out}(\omega) + E_{y,out}(\omega)E^*_{y,out}(\omega) = R(\omega)E_{in}(\omega), \tag{7.41}$$

which for the case of no amplitude modulation results in the spectrum of E_{in}. This connection is portrayed in Fig. 7.10 with an experimental (a) and a simulated spectrum (b). The sum-spectra of the two orthogonal components are shown in the top right insets, which resemble a Gaussian shape, as Eq. 7.41 predicts. The simulation also incorporates the angle dependent reflection efficiency of the gratings, as it was not (yet) corrected, it manifests as small dips in the sum-spectra.

7.5 Pulse forms employing amplitude modulation

The new possibilities of the serial setup provided by incorporation of the amplitude will be demonstrated in the following. First, amplitude modulation will be used to compensate for the grating effect on a pixel-per-pixel basis (Sec. 7.3.1), later, the effects of a stronger amplitude modulation will be inspected.

7.5.1 Application of grating precompensation

Fig. 7.11 (a) shows another linear/circular double pulse with Δt=500 fs, but with a grating correction transmission mask as pictured in (b). The fence structure originates from the difference retardance pattern required to create such a pulse, and

[16]Simulation tells that this particular side pulse has opposite helicity respective to the main circular sub pulse and should face downwards.

[17]which will be discussed in detail in Sec. 7.6, Eq. 7.37

[18]where the linear pulse points towards 0°, no amplitude modulation was applied, using the grating equalizing method

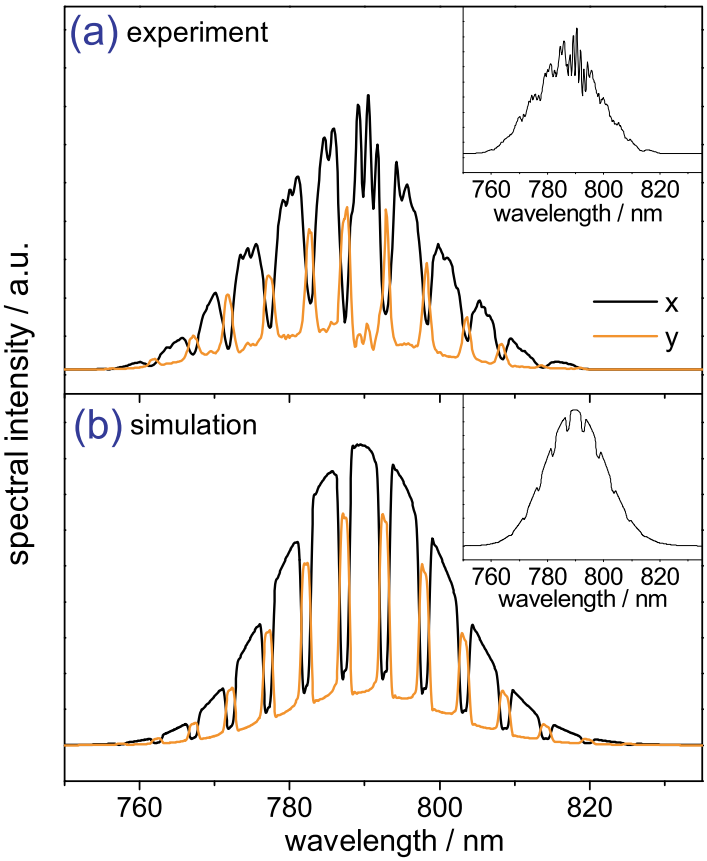

Figure 7.10: Measured (a) and simulated (b) spectral intensities for a double linear/circular pulse form (Δt=400 fs), created without amplitude modulation. Right-top insets: sum spectra of the two orthogonal components.

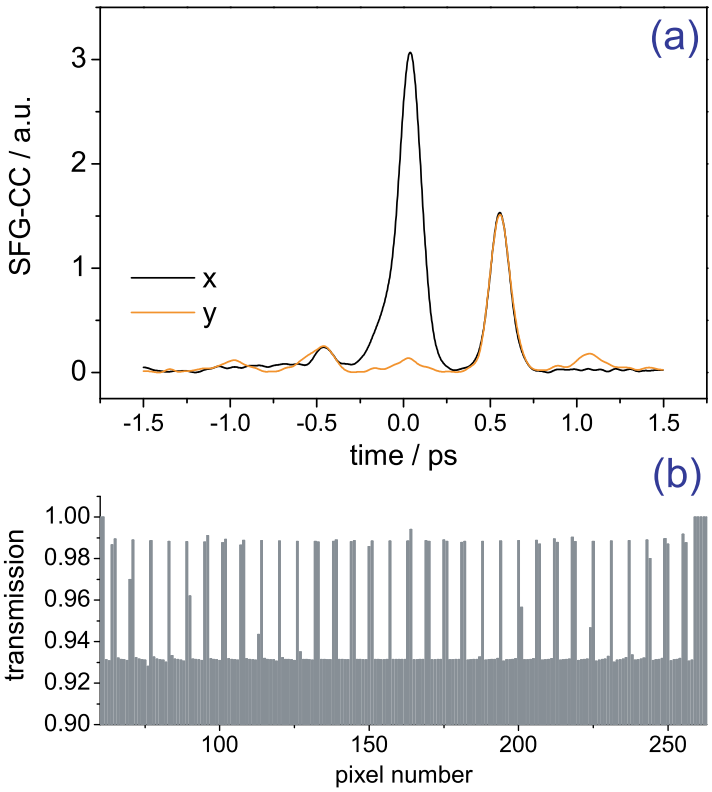

Figure 7.11: Linear/circular double pulse (a) with $\Delta\phi = -0.5\pi$ and Δt=500 fs, using an adequate correction pattern (b) for such a pulse form, obtained from the lookup-table created by inverting and normalizing the grating efficiency scan P_{WO} from Fig. 7.5.

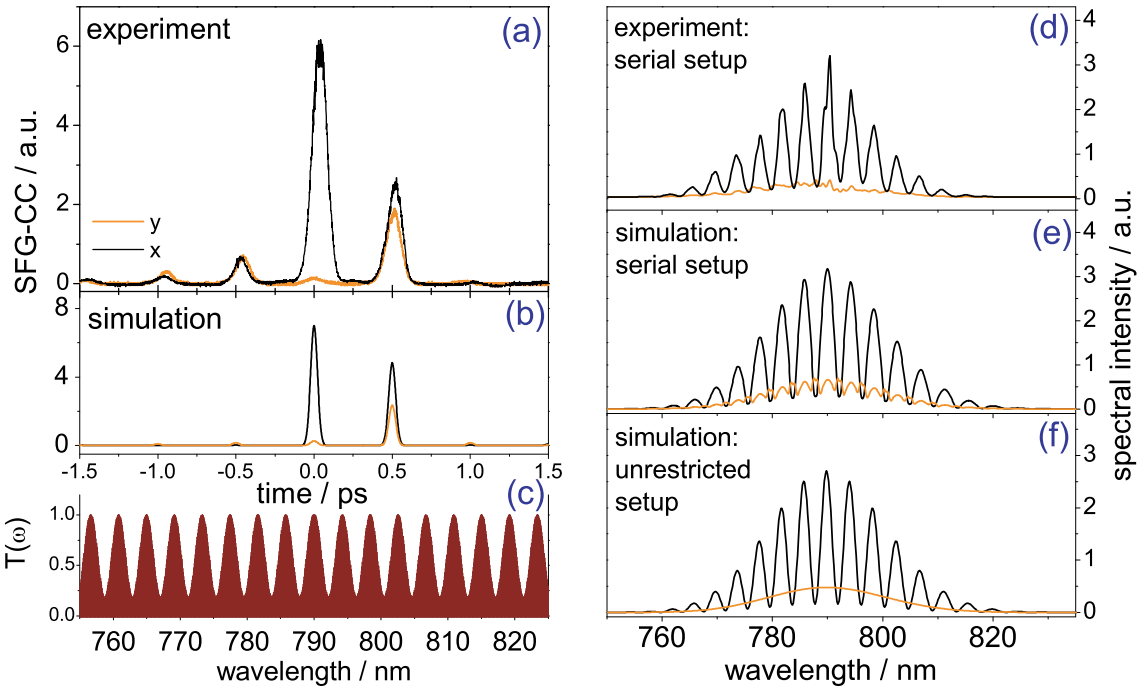

Figure 7.12: Pronounced amplitude modulation for a $\Delta t = 500$ fs linear/circular double pulse. Graph (a) is the measured, (b) the simulated SFG-CC intensity, with no significant distortion when the transmission pattern (c) is applied. The curves (d) and (e) are the measured and simulated spectra; and (f) is the spectrum, which an unrestricted pulse shaper setup would produce.

was derived from the look-up-table (see Sec. 7.3.1). This way, no $\Delta\phi$ adaptation is necessary to create the correct ellipticities, allowing to use the appropriate $\Delta\phi = \pi/2$ for circular pulses, demonstrating that it is possible to use the amplitude precompensation method also for more complex pulse shapes.

7.5.2 Sum-intensity amplitude modulation

As the real parts of the retardances (Eq. 7.37) were determined to be independent of the amplitude $R(\omega)$, there is some choice of selecting transmission patterns. From all the possible patterns, the one which corresponds to the sum-intensity

$$R^2_{sumI}(\omega) = T_{sumI}(\omega) = \frac{|E_{x,out}(\omega)|^2 + |E_{y,out}(\omega)|^2}{|E_{in}|^2} \tag{7.42}$$

was chosen to be tested experimentally. This pattern is related to the waveform as it incorporates the same amplitude "modulation frequency" as a double pulse of this distance[19].

Fig. 7.12 gives a demonstration for a linear/circular $\Delta t = 500$ fs double pulse; the transmission pattern which is applied, is drawn in (c). The temporal pulse form - (a) measured and (b) simulated - is not significantly distorted when comparing to the amplitude-free cases presented earlier, there is "only" a loss of circularity for the pulse at t=520 fs, with still all side pulses present. The intensity sums of the two

[19] see also Fig. 6.5, third row

perpendicular component spectra do no longer match the input pulse's shape alone, but are modulated with the transmission pattern.

Involving the amplitude can be seen as a step towards an unrestricted setup which is able to invoke the filter from Eq. 7.30 (which would also produce a side pulse-free temporal pulse form), depicted in Graph (f). The unmodulated Gaussian shape for the y-component (gray) originates from the orthogonality of the linear pulse for this component. As it lies in the x-plane, it has no component in y, and therefore causes no spectral interference. Comparing (e) and (f) and the amplitude-unmodulated case from Fig. 7.10 (whose sum-intensity must yield a Gaussian for every frequency), the advantages of the serial setup become more transparent as the applied transmission reduces the picket-structure of the y-component, letting it look like more like the unrestricted case.

7.6 General temporal pulse forms with the serial setup

The serial shaper's capabilities to create more general temporal pulse forms will be studied in the following. Spectral restrictions do not prohibit interferences of different pixels/frequencies to other states when rejoined in the time domain [148]. This effect is abundantly utilized in the literature while performing free optimization experiments which result in very complex waveforms in time [139, 142]. As it is the focus of this work to generate custom-tailored pulse forms, a study of the effects of the spectral restrictions in the time domain is required.

7.6.1 Attempt at arbitrary pulse forms

To explore the limitations of temporal shapes of the serial setup, an arbitrary, parametric pulse in time is created in order to learn about the serial response $\mathbf{E}'_{out}$ (Eq. 7.38) which transforms the desired input parameter set $\{I,\ H_{ba},\ \beta/2\} \rightarrow \{I',\ H'_{ba},\ \beta'/2\}$. For the following, amplitude modulation was omitted, so the results also represent a single-pass through a $\pm 45°$ setup.

Fig. 7.13 shows snapshots (top to bottom) of parameter scans of the (simulated) three-dimensional electrical field for three different parameters, major axis rotation (a), intensity (b), and ellipticity (c). For all cases, a double pulse[20] is constructed, one parameter of the sub pulse P_1 at t=200 fs (yellow, marked by an arrow) is changed, and the effect on the pulse form $\mathbf{E}'_{out}$ is studied.

Axis rotation. Fig. 7.13 (a) shows the simulated results for E'_{out} for a major axis rotation, with snapshots taken in 10° steps. When going through the pictures, it becomes apparent that P_2, which is not supposed to change, varies in orientation; it skews around the x-axis and only shows correct results for 0° and 90°; similarly happening to the side pulses. Quantitatively, the parameter couplings for this particular double pulse are depicted in Fig. 7.14. In Graph (a), the angle skewing and the P_1 dependent major axis angle of P_2 are pictured; whereby the dashed lines represent the weaker side pulses. It can also be seen that the desired angle for P_1 could

[20] Δt= 200 fs, λ_0=786.7 nm, and FWHM=22 nm

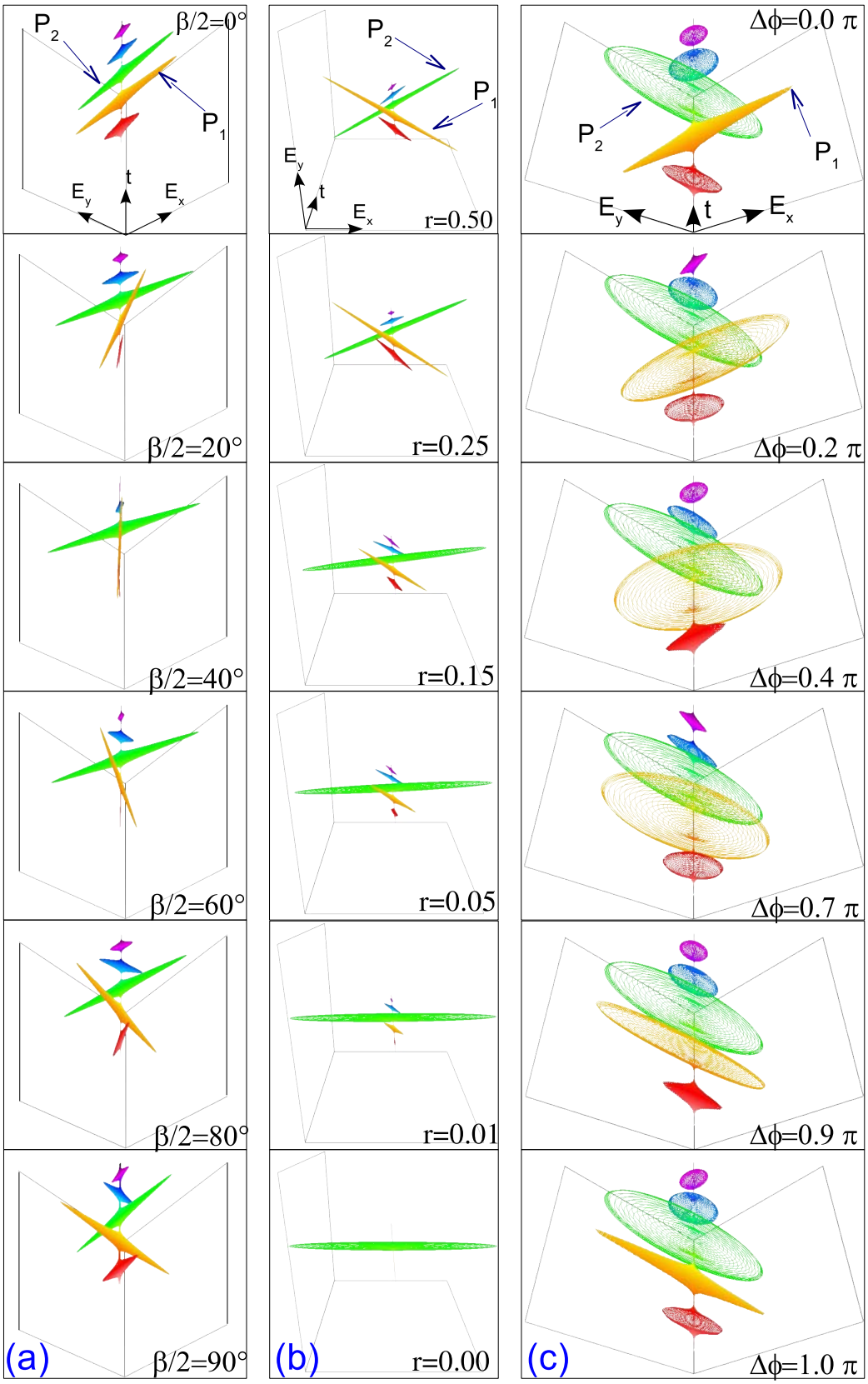

Figure 7.13: Simulated scans for (a) major axis angle, (b) intensity, and (c) $\Delta\phi$ - the restricted case - for a double pulse scenario. The two major features P_1 and P_2 are marked by arrows and discussed in the text.

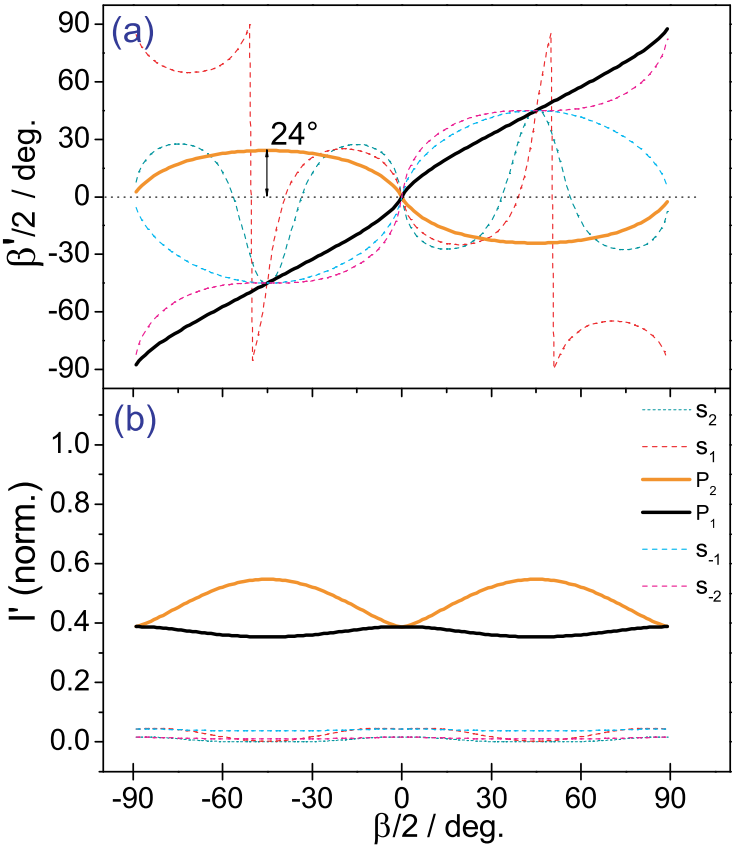

Figure 7.14: Angular scan of P_1. The resulting angles of the other pulses are plotted in (a), the intensity response in (b). Thick black line: P_1', gray line: P_2'; dashed thin lines: side-pulses (labelled s_{-2} to s_2).

be achieved except for some slight deviation (black, slightly twisted, but otherwise straight line). P_2 can be seen to pivot around the x-axis with a maximum elongation of 24°. The simulations also show that there is an ongoing redistribution of all sub pulse energies, which is shown in Fig. 7.14 (b), which means that also the sub pulse energies are coupled to each other.

Intensity/Energy change. Fig. 7.13 (b) is intended to show the transition from the multi-pulse to the unshaped single pulse "domain". Starting with an (intended) 0° and 30° linear/linear double pulse (P_1 and P_2), respectively, $r = R_1^2/R_2^2$ is changed until P_1 disappears. This can be similarly seen in Fig. 7.15 (a): when P_1 diminishes (black line) and P_2 grows in intensity due to energy conservation as no amplitude modulation was applied. More interesting is the angular "collapse" of P_2 towards 0° (small arrow), as shown in Graph (b), where the pulse form is "closing in" to the single-pulse angular restriction, and the desired 30° could only be upheld till some point.

Restricted parameters, ellipticity scan. The spectral limitations of the serial setup increase the difficulty of systematic parameter scans by a substantial degree, so for the implementation into the evolutionary algorithms, arbitrary major axis were, as a consequence, not utilized. When the pulse's major axes are restricted to 0° and 90°, Eq. 7.1.2 has to be rewritten to read

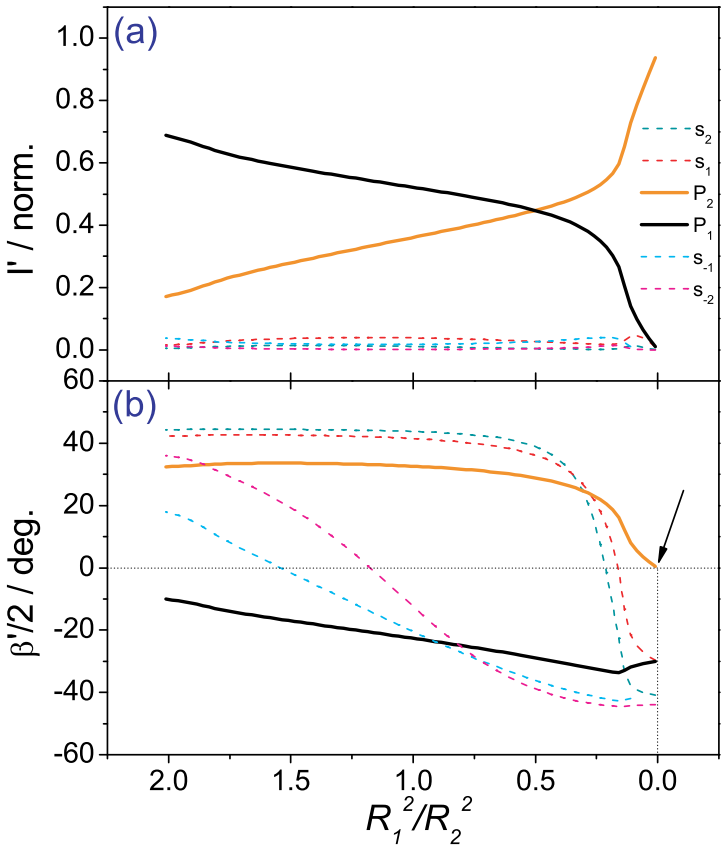

Figure 7.15: Single-pulse limit for arbitrary major axes: (thick black line: P_1, gray line: P_2; dashed, thin lines: side-pulses s_{-2} to s_2). Graph (a) shows the desired intensity ratio versus obtained intensity ratio while one P_1 is "turned off" and (b) depicts an angular "destabilization" when the intensity of P_1 is no longer high enough to allow interference to other major axis angles than 0° or 90° (see arrow).

$$\begin{aligned} a^2 &= I \cdot \cos^2 \tfrac{\Delta\phi}{2} \\ b^2 &= I \cdot \sin^2 \tfrac{\Delta\phi}{2} \\ \varepsilon &= sgn(\sin \tfrac{\Delta\phi}{2}) \cdot \tfrac{\pi}{2}. \end{aligned} \tag{7.43}$$

Similar to the parameter scans before, the ellipticity is changed, but this time with the above stated restrictions. For the demonstration, a Δt = 200 fs elliptical/elliptical double pulse is used, with an elliptical P_2 ($\Delta\phi$=0.8 and H_{ba}=0.325), while P_1's $\Delta\phi$ is changed.

The outcome is shown in the snapshots in Fig. 7.13 (c) from $\Delta\phi$=0 - π, and as parameter scan in Fig. 7.16. The outcome is that now, for the restricted parametrization, P_1 and P_2 are no longer linked. Except for the behavior of the side pulses (where the largest is about 1/10 of the main pulse's intensity), the difference retardance maps nicely on the ellipticity (thick, triangular black curve), while the ellipticity of the first pulse stays unchanged (flat gray line) at H_{ba} = 0.325, as intended.

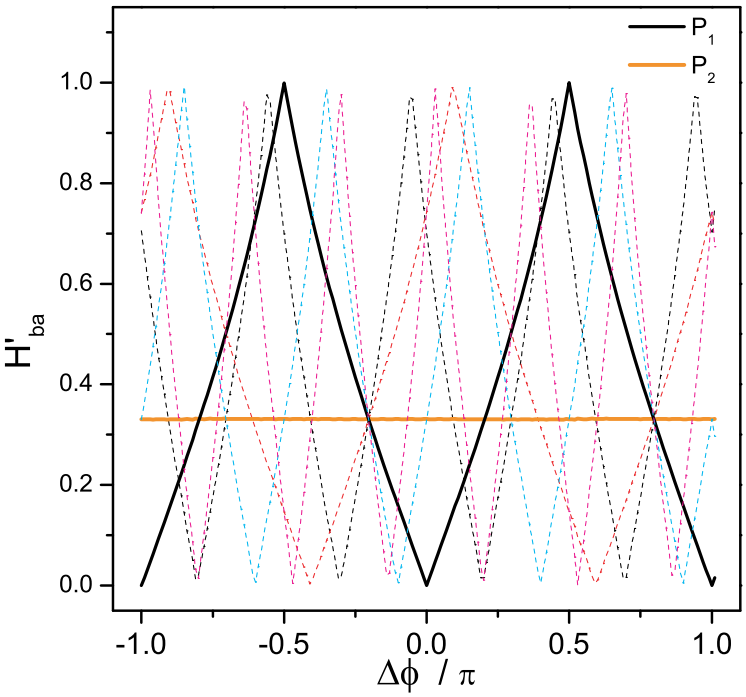

Figure 7.16: Elliptical major axis locked to 0° and 90° degrees, except for the side-pulses. Thick black line: axes ratio of the pulse to be changed (double elliptical - see text), thick gray line: ellipticity of the other major pulse, thin dashed lines: side-pulses.

7.6.2 Side pulse-free fields

Fig. 7.17 (a) shows the 3D electrical field of an overlapping, near-linear double pulse in the ±45° system, where one of the sub pulses is also negatively chirped with -1400 fs^2, resulting in a change of major axis angle in the overlapping part. Interestingly, there are no signs of side-pulses, even on the prolonged t axis. The explanation is as follows: For fields where the general solution of Eq. 7.34 for the retardances obeys

$$\Im[\tilde{\phi}_{a,b}(\omega)] = \Im\left[-i \ln \frac{E_{out,x}(\omega) \pm E_{out,y}(\omega)}{E_{in}(\omega)}\right] = 0 \tag{7.44}$$

(see also Eq. 7.36), meaning if all imaginary retardance components for a supposed field vanish, it can be obtained exactly with the serial setup, as it automatically obeys the limitations of the spectral domain. For experimental purposes it might suffice if the imaginary term is small; to demonstrate that the depicted waveform is indeed a special case, one sub pulse is changed to +55° - Fig. 7.17 (b) - and as a matter of fact, a small side pulse appears on the opposite side (indicated by the arrow).

7.7 Restricted example pulses

As custom-tailored polarization pulses will be incorporated into the evolutionary algorithm, a short overview with a few selected pulse forms will be given, whereby the polarization control parameter $\Delta\phi$, with the restrictions of Eq. 7.43 shall be emphasized.

Fig. 7.18 presents a selection of example pulses, where for reasons of simplicity, only the $x-$ and $y-$ projections of the SFG-CCs are shown. The example pulses are all double pulses with varying distances, intensities, chirps, and some special

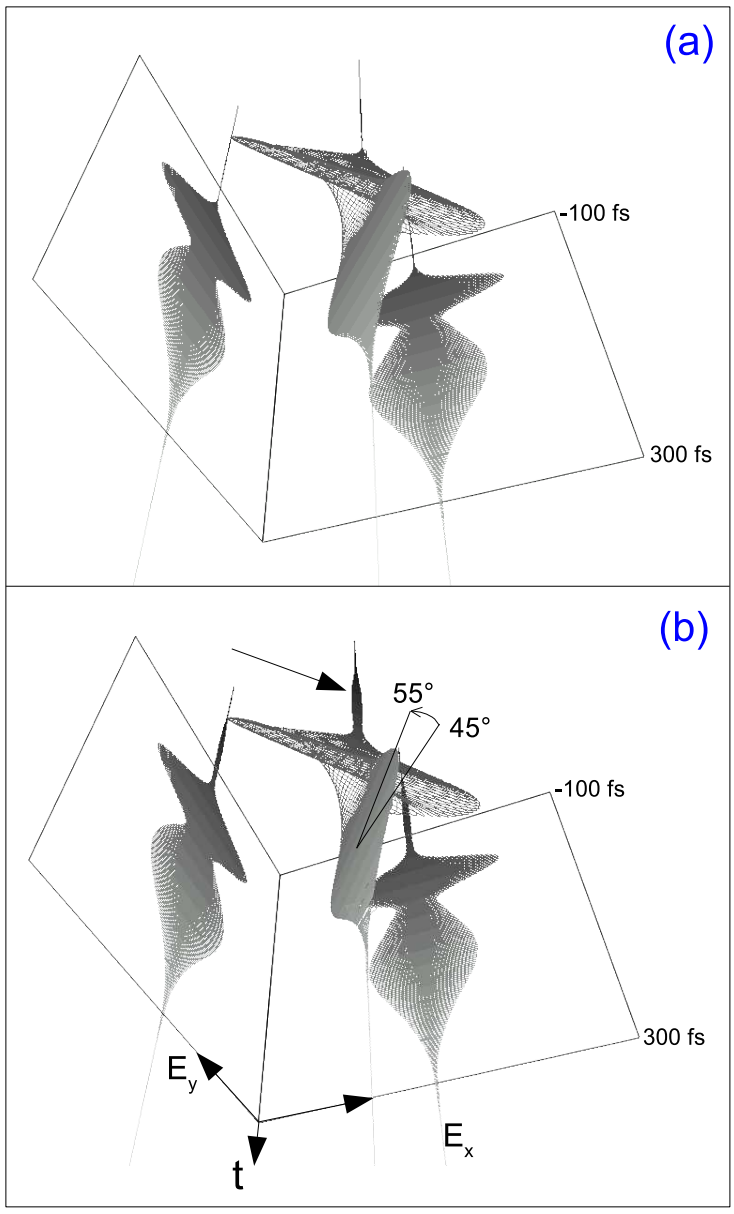

Figure 7.17: Simulation of a side pulse-free double pulse using the serial setup, consisting of two overlapping, ±45° aligned linearly polarized pulses; one of them has a linear chirp of -1400 fs^2. (b) A slight rotation to 55° of one of the sub pulses already produces a side pulse (see arrow).

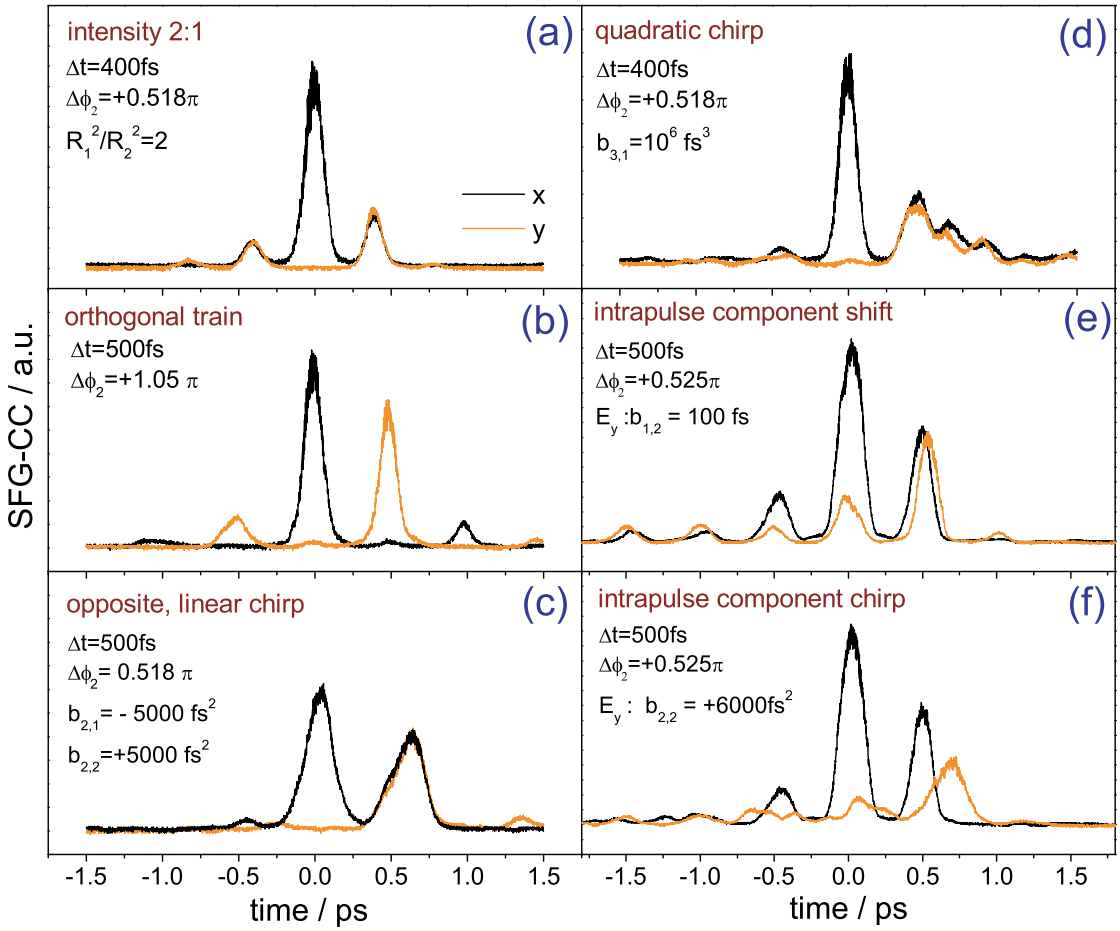

Figure 7.18: Selected experimental example pulses created by the serial setup, demonstrating a few of the new possibilities with the polarization control parameter $\Delta\phi = \phi_a - \phi_b$.

features; the respective parameter values are also noted in the respective graphs.

In (a), the ratio R_1^2/R_2^2 of the sub pulses was chosen to be 2:1, resulting in a weaker circular pulse at t=400 fs. Alternating, orthogonal linear pulses are demonstrated in (b); note that the side pulses show a similar, alternating behavior. (c) shows alternating chirps of $b_2 = \mp 5000$ fs^2 for the linear first and circular second sub pulse, respectively, which shows that both linear and circular pulse are broadening in time by the same amount. Graph (d) demonstrates a quadratic spectral chirp of $b_3 = 10^6$ fs^3 of the circular pulse, which manifests itself by a short, circular pulse train following the pulse. The next two examples go beyond the implemented parametrization, but indicate interesting possibilities. Graph (e) shows the potentiality to shift sub pulse components separately in time, in this case, the y-component of the circular pulse was displaced by 100 fs which creates intriguing intra-pulse ellipticity states. For the last example, the $y-$component of the circular pulse alone was brought to exhibit a linear chirp of +6000 fs^2 and a time shift, which results in simultaneous ellipticity and instantaneous-frequency changes within a single pulse.

7.8 Parametric polarization shaping on NaK

Having polarization shaped femtosecond laser pulses opens a new dimension for coherent control experiments, as it provides light fields which can be tailored to ideally interact with molecule's dipole moments. It enhances transitions which would otherwise have a low ionization probability as the projection of the electrical field at the dipole moment would be small.

7.8.1 Interaction of polarized pulses with linear molecules

The disturbance of the time-dependent Hamiltonian H_1 depends on the scalar product of the electrical field and the molecular dipole moment $-\mathbf{E}(t)\cdot\boldsymbol{\mu}$. To calculate the excitation probability, the projection of the field on the dipole moment is the decisive factor. Transitions in dimers may require polarizations which are either parallel or perpendicular to the molecular axis. This is governed by parity selection rules; the odd parity of the electric dipole moment operator requires that the initial and final orbitals have a different parity, otherwise the matrix element $<\psi_i|\mathbf{E}\cdot\boldsymbol{\mu}|\psi_k>$ vanishes. If the quantum number Λ, the projection of the total electronic angular momentum onto the internuclear axis, is a good quantum number and does not change during a transition, the transition is said to be parallel, like for $\Sigma \leftarrow \Sigma$ or $\Pi \leftarrow \Pi$ transitions; if Λ changes by ± 1, a perpendicular transition (respective to the internuclear axis) is at hand.

When a sample of randomly aligned molecules is irradiated with linearly polarized light, an ensemble is selected which has their transition dipoles aligned to the incoming polarization [152] which is called photoselection. For NaK, the ionic state can be reached[21] by a two-photonic transition from the first excited $A(2)^1\Sigma^+$ state via the resonant, intermediate $A(6)^1\Sigma^+$ state (a $\Sigma \rightarrow \Sigma$ transition), or via the $B(3)^1\Pi$ state (which is a $\Sigma \rightarrow \Pi$ transition). A polarization shaped pulse which changes its polarization direction on a femtosecond timescale, is too fast for the molecule to adapt (align) to the field, and is considered to be a non-adiabatic transition.

The alignment of molecules has been shown to be accessible by the polarization of high-intensity pico- and femtosecond pulses, for example N_2, where the multiphoton ionization was found depend on the ellipticity [153]. A pre-aligned molecular sample would result in a better controllability [140, 154, 155], but even with more or less isotropic starting conditions as in a molecular beam, an effect can be established when multi-photon transitions are involved. Starting with the transition dipole matrix element

$$M_{ik} = \int \psi_i e\mathbf{r}\psi_k d^3r \tag{7.45}$$

it can be shown that for for single photon transitions using linearly polarized light, the transition probability is proportional to

$$P^{\omega}_{lin} \propto M_{ik}E_0^2\cos^2\theta \tag{7.46}$$

whereby θ is the angle between the field direction and the dipole moment. When integrating probability over all polar and azimuthal angles the number of excitations

[21] for a potential scheme see Fig. 4.1 from Chapter 4

can be estimated. For single photon transitions, however, linearly or circularly polarized light of the same intensity yield the same result, when the sample is initially randomly aligned, the difference lies only in their final distribution, whereby the linear excitation is directionally selective.

For molecules that feature transitions that require different polarizations during multi-photon processes on a femtosecond timescales where there is not enough time for the molecule to adiabatically align it can be shown that the effect of polarized light is not averaged out. If a $\parallel \rightarrow \perp$ transition is irradiated with a linear, perpendicular double pulse (with the right distance to match the Franck-Condon conditions at the outer turning point), a theoretical improvement by the factor of two could be reached when compared to a double pulse which is only linearly polarized [139].

7.8.2 Free and PAP optimization of NaK

For the comparisons, the following abbreviations will be used: Depending on the employment of phase, amplitude, and polarization, three letters (like PAP for phase, amplitude, and polarization, or just phase PXX) will designate the type of experiment. As a light source, the amplified laser system at the center wavelengths of 782 nm and 794 nm (FWHM bandwidth 22 nm) was employed, using the Coherent RegA with pulse energies of about 400 nJ per pulse at the apparatus.

For a first experiment, a phase-only optimization is performed to yield a reference optimization factor to compare with the results from polarization-enabled optimizations. The obtained waveform is displayed in Fig. 7.19 (a) and had the factor 1.79± 0.04. This is already quite high compared to earlier results which were obtained with non-amplified pulses and at narrower bandwidths [77]. The pulse structure obtained (measured by two orthogonal SFG-CCs) shows a central complex with many small, temporally not fully separated sub pulses, whose peaks can indeed be assigned to multiples of $1/2 \cdot T_{osc}$ of a wavepacket on the first excited state, which has been observed throughout this work, and is theoretically well established due to resonance conditions and Franck-Condon factors [133], and it is safe to attribute it to a stepwise excitation scheme [79].

For the next, free optimization experiment, a PAP encoding is used which is potentially able to generate very complex pulse forms in time by interference, including major axes angles besides 0° and 90° in the time domain. The results are shown in Fig. 7.19 (b), offering an additional 19% increase to the factor of 2.130 ± 0.005 compared to the already high PXX factor. Interestingly, the outcome can be interpreted as a multi-step excitation with alternating, and predominantly linearly polarized pulses with major axes of 0° and 90°, which was neither an explicit nor implicit requirement[22]. Every sub pulse is followed by an orthogonal pulse, in total seven times. The perpendicular sub pulse's distances all fit very well to $1/2 \cdot T_{osc}$ which suggests a scheme of a repeated, stepwise excitation, including to a high degree of certainty the orthogonal $B(3)^1\Pi \leftarrow A(2)^1\Sigma^+$ and $A(2)^1\Sigma^+ \leftarrow X(1)^1\Sigma^+$ transitions to obtain the higher optimization factor.

[22]it should be mentioned that similar alternating, perpendicular structures were also observed to a major part of the inferior runs

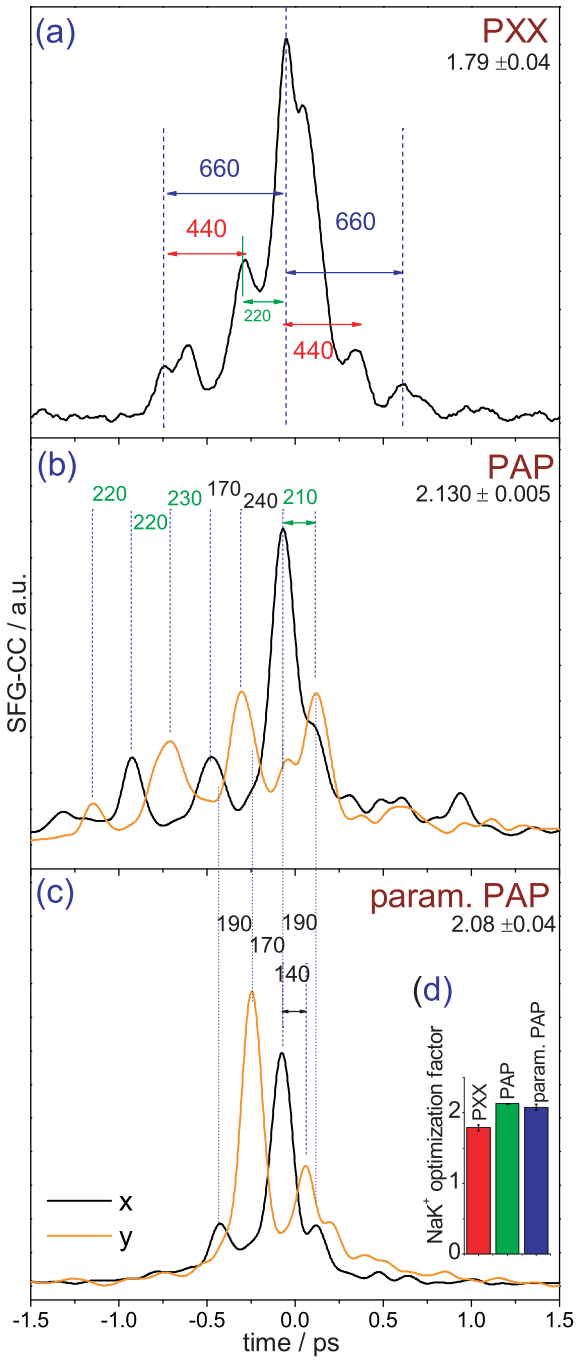

Figure 7.19: Optimization results for NaK at 782 nm with free PXX (a), free PAP (b), and a parametric PAP encoding (c), with the factors (d). Graph (a) and (b) were already shown in Ref. [28].

7.8.3 Parametric PAP optimization

To avoid too complex results, only double pulses will be employed for the following experiments. More complex shapes like triple pulses could lead to collisions - meaning interferences - of side pulses with intended pulses, leading to greatly distorted polarization states and additional parameter couplings. As a result of the experiments and considerations conducted earlier in this chapter, the parametrization used for the NaK ionization experiments with polarized pulse forms will be

$$\vec{x} = \left\{b_{0,1}, b_{0,2}, b_{1,1}, b_{1,2}, R_1^2, R_2^2, \Delta\phi_1, \Delta\phi_2\right\}, \tag{7.47}$$

which implicitly contains the axis restriction[23]. As parallel and perpendicular electronical transitions should be preferred as ionization paths for the examined molecule, the restriction should not pose a fundamental obstacle. The amplitude was incorporated using the sum-intensity (Eq. 7.42). The limits for the encoding were two sub pulses, while P_1 was supposed to stay at t=0 fs. The position of P_2 was limited to [-1000,-100] fs, R_1^2/R_2^2 was set to lie within [0.1,1], the zero order phase b_0 within $[-\pi;\pi]$, and $\Delta\phi_{1,2}$ within $[-\pi;\pi]$.

Already after 28 generations (instead of 126 for the free optimization), convergence was reached. The optimized SFG-CC pulse form is shown in Fig. 7.19 (c) having a factor of 2.08 ± 0.04, which is quite close to the one from free optimization, 2.13, but with a greatly reduced temporal complexity. The pulse distance of the main sub pulses is about 170 fs, which is less than 0.5 T_{osc}, with side pulse distances of each 190 fs. Their x- and y-component at peak are nearly mutually exclusive, which implies a high degree of orthogonality; there is a qualitative similarity to the results from the PAP optimization with respect to the orthogonal, sequential sub pulses (dashed vertical lines). The parametric pulse manages a high ion yield with only four distinguishable sub pulses (including the side pulses) instead of eight, which the PAP optimization provided. The different shapes and therefore quantitatively different wavepacket dynamics initiated by the parametric solution are to the most part due to the implicit restrictions of the parametric case, locking the side pulses to the main pulses and prohibiting, for example, asymmetric side pulse locations[24]. It having still a very high optimization factor therefore would make this particular shape worthy of further (theoretical) study.

When comparing the convergence speed of the parameters with a course analysis, the sub pulse's $\Delta\phi$, related to the ellipticity, is the one to converge the earliest - Fig. 7.20 (d). The $\Delta\phi = \pm\pi$ "jumps" until generation 15 can be interpreted as undecidedness towards left- or right-handedness, which is, however, of no great importance for near-linear polarization states. The b_0 development (c) seems to be quite steady, the pulse's relative energies (b) need 18 generations to settle down to the final value and are still exhibiting a certain "jumpiness", which probably originates from the fact that two competing niches/solutions with different peak intensities have approximately the same ion yield. The pulse distance (a) seems to only gradually converge to the final value, which is most likely due to the strong coupling to the side pulse distances and intensities (as discussed in Section 7.6).

[23] when substituting $\Delta\phi_N$ into Eq. 7.43, whereby the R_N^2 correspond to I

[24] see also Fig. 7.9

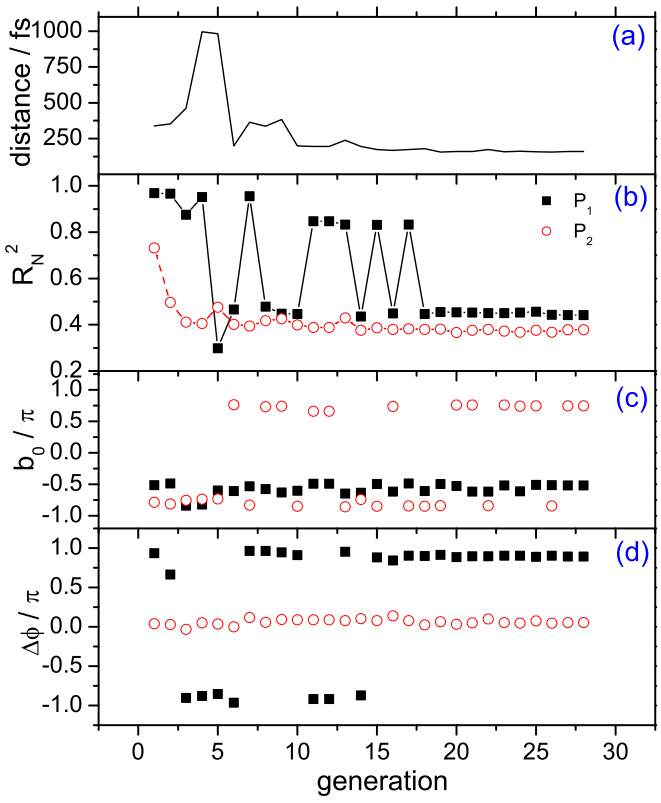

Figure 7.20: Course analysis for the optimization depicted in Fig. 7.19 (c). Graph (a) shows the development of the sub pulse distance between the main pulses, (b) the sub pulse intensity (proportional to R_N^2), (c) the zero order phase, and (d) the difference retardance $\Delta\phi$, which is closely connected to the ellipticity; showing orthogonal, linearly polarized states ($\Delta\phi$=0, $\pm\pi$).

7.8.4 Parametric PXP optimization

For the next optimization, another central wavelength (λ_0=794 nm) is chosen, where optimization factors generally are lower, as known from Ref. [77]. The difference to the previous parametrization is the disabled amplitude modulation; all other boundary conditions are the same as before. As always, the side pulses take part in the optimization process, resulting in a triple-pulse structure (Fig. 7.21) with perpendicular, not too elliptical sub pulses, and offering an optimization factor of 1.390 ± 0.004. The optimized pulse again admits a simple ionization scheme because the sub pulse distances of 260 fs and 270 fs are again not too far - considering their length - from 0.5 T_{osc}. The first pulse (t=60 fs) excites a ground state wavepacket to the A(2)$^1\Sigma^+$ state, the second perpendicular sub pulse (t=320 fs) ionizes the molecule via the intermediate, perpendicular B(3)$^1\Pi$ state at the outer turning point, while simultaneously creating population, which is again ionized by the perpendicular third pulse (t=590 fs).

Inner turning point exclusion. In the last example for parametric shaping, the freedom of choosing physically motivated boundary conditions will be put into action by restricting the pulse distance to exclude ionization at the first wavepacket round-trip. This can be seen as "question" to the system which it tries to solve by optimizing the ionization with a [-1000,-400] fs distance restriction, with otherwise the same settings as in Fig. 7.21 (a).

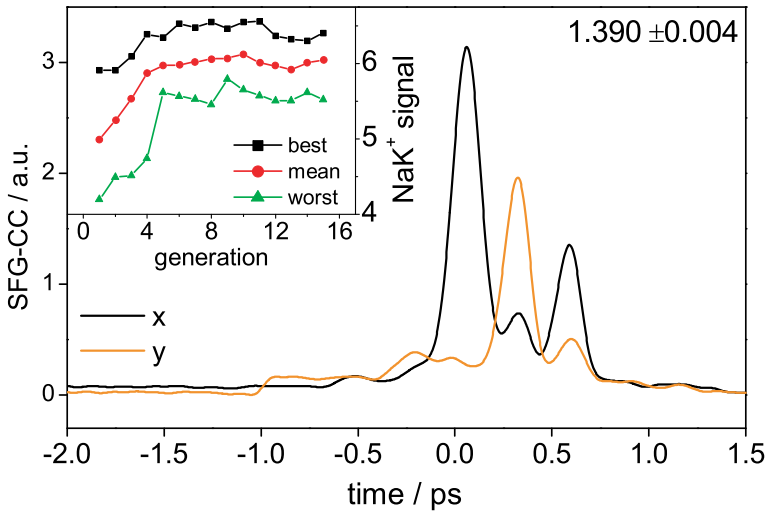

Figure 7.21: Parametric PXP optimization results, featuring near-linear, orthogonal sub pulses with distances of 260 fs and 270 fs. The left top inset is the learning curve, displaying the best, mean, and worst individual during the run.

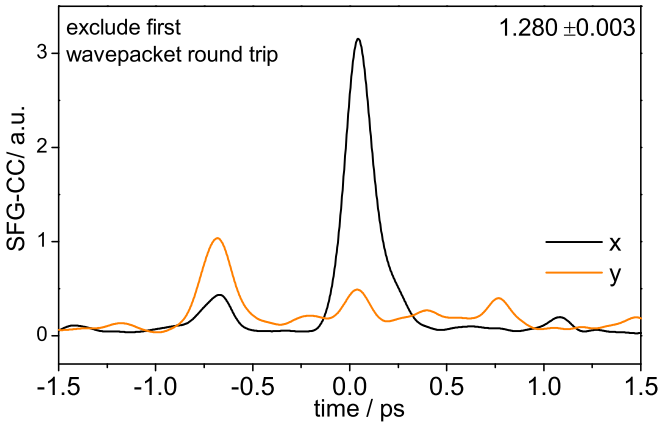

Figure 7.22: Parametric PXP optimization, with temporal boundary conditions set in order to exclude the first round-trip of the wavepacket, featuring a distance of 710 fs, close to $1.5 \cdot T_{osc}$.

Fig. 7.22 shows the result, which yields an optimization factor of 1.28±0.003. As consequence of the restriction, a sub pulse distance of $1.5 \cdot T_{osc}$ is obtained, permitting an ionization scheme where the population created by the first pulse is ionized by a two-photon transition at the outer turning point after 1.5 round trips by the perpendicular, more intense pulse.

7.9 Summary

In this chapter, polarization shaping with an emphasis on the time domain using a recently developed pulse shaper setup that incorporates phase, amplitude, and polarization was presented. The added amplitude was shown to be a manageable parameter which provides a new degree of control for femtosecond polarization shaping experiments, for example by addressing specific vibrational transitions. Except for the occurrence of side pulses (which are due to the spectral phase lock of the x- and $y-$component), it was shown that the coupling of pulse parameters can be

reduced if specific restrictions to the major axes are upheld. The findings from the optical studies were taken into account when choosing new control parameters for the evolutionary algorithm. The different parametrization experiments demonstrated a controllability of the experimental outcome and the ionization path, while still upholding relatively high optimization factors, and most importantly, simplicity of the obtained waveform. They also featured customized search space restrictions and an improved convergence speed. The resulting pulse shapes allow to assign an interesting ladder-climbing process with alternating, orthogonal sub pulses at multiples of half the oscillation period of the first excited Σ state of NaK, strongly indicating consecutive $\Sigma \leftrightarrow \Sigma$ to $\Pi \leftrightarrow \Sigma$ transitions along the ionization path. The experiments with the serial setup including its potentialities and shortcomings motivated the construction of another pulse shaper setup which will be discussed in the next chapter.